Disrupting Integrator complex subunit INTS6 causes neurodevelopmental disorders and impairs neurogenesis and synapse development

Xiaoxia Peng[1,2,*], Xiangbin Jia[1,2,*], Hanying Wang[1,2], Jingjing Chen[1,2], Xiaolei Zhang[1,2], Senwei Tan[1,2], Xinyu Duan[3], Can Qiu[1,2], Mengyuan Hu[1,2], Haiyan Hou[1,2], Ilaria Parenti[4], Alma Kuechler[4], Frank J Kaiser[4,5], Alicia Renck[6], Raymond Caylor[7], Cindy Skinner[7], Joseph Peeden[8], Benjamin Cogne[9,10], Bertrand Isidor[10], Sandra Mercier[9,10], Gael Nicolas[11], Anne-Marie Guerrot[11], Flavio Faletra[12,13], Luciana Musante[14], Lior Cohen[15,16], Gaber Bergant[17], Goran Čuturilo[18,19], Borut Peterlin[17], Andrea Seeley[20], Kristine Bachman[20], Julian A. Martinez-Agosto[21], Conny van Ravenswaaij-Arts[22], Dennis Bos[22], Katherine H. Kim[23], Tobias Bartolomaeus[24,25], Zelia Schmederer[24,25], Rami Abou Jamra[24], Erfan Aref-Eshghi[26], Wenjing Zhao[27,28], Yongyi Zou[29], Zhengmao Hu[1,2], Qian Pan[1,2], Faxiang Li[1,2], Guodong Chen[1,2], Jiada Li[1,2], Zhangxue Hu[3], Kun Xia[1,2,30,#], Jieqiong Tan[1,2,31#], Hui Guo[1,2,#]

[1]Hunan Key Laboratory of Medical Genetics, Hunan Key Laboratory of Animal Models for Human Diseases, MOE Key Lab of Rare Pediatric Diseases, Center for Medical Genetics, School of Life Sciences, Central South University, Changsha, Hunan, China; [2]Furong Laboratory, Changsha, Hunan, China; [3]Department of Pediatrics, Daping hospital, Army Medical University, Chongqing, China; [4]Institute of Human Genetics, University Hospital Essen, University of Duisburg-Essen, Essen, Germany; [5]Center for Rare Diseases (Essener Zentrum für Seltene Erkrankungen, EZSE), University Hospital Essen, Essen, Germany; [6]Dricoll Children's Hospital, Corpus Christi, TX, USA; [7]Greenwood Genetic Center, Greenwood, SC, USA; [8]East Tennessee Children's Hospital, The University of Tennessee Department of Medicine, Knoxville, Tennessee, USA; [9]Nantes Université, CHU de Nantes, CNRS, INSERM, l'institut du thorax, F-44000 Nantes,

France; [10]Nantes Université, CHU de Nantes, Service de Génétique médicale, F-44000 Nantes, France; [11]Univ Rouen Normandie, Normandie Univ, Inserm U1245 and CHU Rouen, Department of Genetics and reference center for developmental abnormalities, F-76000 Rouen, France; [12]Institute of Medical Genetics, Azienda Sanitaria Universitaria Friuli Centrale (ASUFC), Udine, Italy; [13]Department of Medicine (DMED), University of Udine, 33100 Udine, Italy; [14]Institute for Maternal and Child Health, IRCCS "Burlo Garofolo", Trieste, Italy; [15]Genetics Unit, Barzilai University Medical Center, Ashkelon, Israel; [16]Faculty of Health Sciences, Ben-Gurion University of the Negev, Be'er Sheva, Israel; [17]Centre for Mendelian Genomics, Clinical Institute of Genomic Medicine, UMC Ljubljana, Šlajmerjeva 4, SI-1000 Ljubljana, Slovenia; [18]Faculty of Medicine, University of Belgrade, 11000 Belgrade, Serbia; [19]University Children's Hospital, 11000 Belgrade, Serbia; [20]Medical Genetics, Geisinger Medical Center, Danville, USA; [21]Department of Human Genetics, Division of Medical Genetics, Department of Psychiatry, Semel Institute for Neuroscience and Human Behavior, Department of Pediatrics, David Geffen School of Medicine at UCLA, USA; [22]University of Groningen, University Medical Centre Groningen, Dept. Genetics, Groningen, The Netherlands; [23]Division of Genetics, Genomics, and Metabolism, Ann & Lurie Children's Hospital of Chicago, Department of Pediatrics, Northwestern University, Feinberg School of Medicine, USA; [24]Institute of Human Genetics, University of Leipzig Medical Center, Leipzig, Germany; [25]Medical Genetics Center (MGZ) Munich, Germany; [26]GeneDx, LLC, Gaithersburg, MD, USA; [27]Department of Medical Genetics, NHC Key Laboratory of Healthy Birth and Birth Defect Prevention in Western China, The First People's Hospital of Yunnan Province; The Affiliated Hospital of Kunming University of Science and Technology, Kunming, Yunnan, China; [28]School of Medicine, Kunming University of Science and Technology, Kunming, Yunnan, China; [29]Department of Medical Genetics, Jiangxi Maternal and Child Health Hospital,

Nanchang, Jiangxi, China; [30]MOE Key Lab of Rare Pediatric Diseases, School of Basic Medicine, Hengyang Medical College, University of South China, Hengyang, Hunan, China; [31]NHC Key Laboratory of Birth Defect for Research and Prevention, Hunan Provincial Maternal and Child Health Care Hospital, Changsha, Hunan, China

[*]XP and XJ contributed equally to this work.

[#]Correspondence: Hui Guo, Center for Medical Genetics and Hunan Key Laboratory of Medical Genetics, School of Life Sciences, Central South University, 110 Xiangya Road, Changsha, Hunan 410078, China. Phone: 086.0731.84805340; Email: guohui2@csu.edu.cn.

Jieqiong Tan, Center for Medical Genetics and Hunan Key Laboratory of Medical Genetics, School of Life Sciences, Central South University, 110 Xiangya Road, Changsha, Hunan 410078, China. Phone: 086.0731.84806749; Email: tanjieqiong@sklmg.edu.cn.

Kun Xia, Center for Medical Genetics and Hunan Key Laboratory of Medical Genetics, School of Life Sciences, Central South University, 110 Xiangya Road, Changsha, Hunan 410078, China. Phone: 086.0731.84806952; Email: xiakun@sklmg.edu.cn.

Conflict of interest: EAE is an employee is and may own stock in GeneDx.

Abstract

The Integrator complex plays essential roles in RNA polymerase II transcription termination and RNA processing. Here, we identify INTS6, a subunit of the Integrator complex, as a novel gene associated with neurodevelopmental disorders (NDDs). Through analysis of large NDD cohorts and international collaborations, we identified 23 families harboring monoallelic likely gene-disruptive or de novo missense variants in INTS6. Phenotypic characterization revealed shared features, including language and motor delays, autism, intellectual disability, and sleep disturbances. Using a nervous-system conditional knockout (cKO) mouse model, we show that Ints6 deficiency disrupts early neurogenesis, cortical lamination, and synaptic development. Ints6 cKO mice displayed a thickened ventricular zone/subventricular zone, thinning of the cortical plate, reduced neuronal differentiation, and increased apoptosis in cortical layer 6. Behavioral assessments of heterozygous mice revealed deficits in social novelty preference, spatial memory, and hyperactivity, mirroring phenotypes observed in individuals with INTS6 variants. Molecular analyses further revealed that INTS6 deficiency alters RNA polymerase II dynamics, disrupts transcriptional regulation, and impairs synaptic gene expression. Treatment with a CDK9 inhibitor (CDK9i) reduced RNAPII phosphorylation, thereby limiting its binding to target genes. Notably, CDK9i reversed neurosphere over-proliferation and rescued the abnormal dendritic spine phenotype caused by Ints6 deficiency. This work advances understanding of INTS-related NDD pathogenesis and highlights potential therapeutic targets for intervention.

Introduction

Neurodevelopmental disorders (NDDs) encompass a heterogeneous group of conditions characterized by impairments in cognitive, social, and motor functions, typically manifesting early

in childhood. These disorders frequently exhibit a broad spectrum of overlapping clinical features (1). The etiology of NDDs is highly complex and multifactorial, with genetic mutations increasingly recognized as substantial contributors. Recent large-scale genomic studies have identified rare *de novo* mutations associated with NDDs, such as autism spectrum disorder (ASD) and intellectual disability (ID), particularly in genes involved in transcriptional regulation, chromatin remodeling, and RNA processing (2-4). Despite advances in genomic research, the genetic landscape of NDDs remains only partially understood due to the broad range of implicated genes and variability in clinical presentations.

The Integrator (INTS) complex is a pivotal multi-protein assembly involved in gene expression regulation, playing essential roles in RNA polymerase II (RNAPII) transcription termination and the processing of small nuclear RNAs (snRNAs) with *de novo* variants recently identified as a cause of neurodevelopmental syndromes (5-8). Comprising 15 core subunits (INTS1-INTS15), the INTS complex mediates RNA processing, ensuring transcriptional fidelity and proper mRNA maturation. These functions are particularly crucial in the central nervous system, where precise gene regulation supports neural development, differentiation, and synaptic plasticity. Although each subunit of the INTS complex contributes uniquely to these processes, the molecular roles of many subunits remain incompletely characterized. While disruptions in transcriptional and post-transcriptional regulatory mechanisms have been linked to NDDs, the specific involvement of the INTS complex in disease pathogenesis has only recently been recognized. Mutations in certain subunits, such as *INTS1*, *INTS8*, and *INTS11*, have been associated with NDDs (9, 10), suggesting that dysfunction of the INTS complex may underlie these conditions. However, for most INTS subunits, the connection with NDDs remains largely unexplored.

In this study, we analyzed genomic data from large NDD cohorts to investigate *de novo* mutations

in all *INTS1-15* subunits and their potential associations with NDDs. We observed significant enrichment of *de novo* variants in *INTS6*, implicating its dysfunction in NDD pathogenesis. To further explore this relationship, we conducted an international, multi-center collaboration to assemble a cohort of cases with *INTS6* variants. These individuals exhibited common NDD phenotypes, including language, social, cognitive, and sleep impairments. Using a conditional knockout mouse model, we demonstrated that loss of *Ints6* disrupts early neurogenesis and RNAPII function. Mice with *Ints6* haploinsufficiency exhibited substantial social and cognitive deficits, along with impaired synaptic development. These findings provide strong evidence linking INTS6 dysfunction to neurodevelopmental outcomes, advancing our understanding of INTS-related pathogenesis in NDDs.

Results

Expression patterns and genetic associations of *INTS* genes with NDDs

The INTS complex comprises 15 proteins encoded by the *INTS1-15* genes. Functional interaction between the INTS complex and Protein Phosphatase 2A (PP2A) coordinates transcriptional and post-transcriptional regulation with phosphatase activity (Figure 1A). *INTS* genes are broadly expressed in the human brain and other tissues, as shown in the Genotype-Tissue Expression (GTEx) dataset (Figure S1). To investigate the temporal-spatial and single-cell expression patterns of INTS genes in the developing human brain, we analyzed the bulk RNA-seq data from the BrainSpan project (https://www.brainspan.org/static/download.html) and a single-cell transcriptome dataset (11). Our analysis revealed that the overall mean expression patterns of *INTS* genes in the BrainSpan dataset is highly express during early brain development that progressively decreases after birth (Figure 1B). These findings indicate that the INTS complex plays a vital role in brain development. Furthermore, single-cell transcriptome analysis demonstrated that *INTS1-*

15 are broadly expressed across various cell types in the developing human brain, further highlighting their potential importance in neural development (Figure 1C).

To examine the association between monoallelic variants in *INTS* genes and NDDs, we analyzed *de novo* variant data from 63,408 probands with NDDs across multiple unpublished and published whole-exome and whole-genome sequencing datasets, including the Simons Foundation Powering Autism Research for Knowledge (SPARK) cohort (12), the Deciphering Developmental Disorders (DDD) cohort (2), the Simons Simplex Collection (SSC) cohort (13), the Autism Sequencing Consortium (ASC) cohort (14), and the MSSNG cohort (15) (see Methods, Table S1). Using a Poisson distribution model (16), we compared the mutation rates of *INTS1-15* in the NDD cohorts with the expected random occurrence rates. Our analysis identified a significant enrichment of *de novo* likely gene-disruptive (LGD) variants in *INTS1* and *de novo* missense variants in *INTS6* among individuals with NDDs ($P_{adj} < 0.05$, Bonferroni correction, Figure 1D, Table S2). While biallelic variants in *INTS1* have previously been linked to NDDs (10), our findings suggest that monoallelic loss-of-function variants in *INTS1* may also contribute to NDD risk. Notably, *INTS6* has not been previously associated with NDDs. Given its novel genetic implication and the constraint observed for both missense and LGD variants (Figure 1D), we focused our subsequent analysis on understanding the role of *INTS6* in NDDs.

Recruitment of a cohort of individuals with *INTS6* variants

To investigate whether *INTS6* variants lead to a novel NDD, we conducted a multi-center international collaboration facilitated by GeneMatcher (17). Through this effort, we identified 21 monoallelic variants within GeneMatcher *INTS6* in 24 affected individuals from 23 families (Table S3). Among these variants, 13 were LGD variants, comprising 6 nonsense, 4 frameshift, and 3 putative splicing variants, identified in 15 families (Figure 2A). Notably, two independent families

carried recurrent variants: p.R610* and c.613+3_613+6del. Functional analysis using a minigene assay revealed that the putative splice-site variant c.613+3_613+6del leads to exon 5 skipping (Figure S2A), while the canonical splice-site variant c.2104+1_2104+8delinsTC results in exon 15 skipping (Figure S2B). In addition to LGD variants, we identified 8 *de novo* missense variants in 9 affected individuals from 8 families, including an identical twin pair (p.S91F) (Figure 2B). All missense variants were located in the N-terminal region of *INTS6*, which is more conserved than the C-terminal, as evidenced by MetaDome analysis and a lower ultra-rare missense variant density in the gnomAD cohort (18) (Figure 2B). Five of the eight missense variants were located within the VWFA domain, which mediates interactions between the Integrator complex and specific genes or transcriptional machinery. These *de novo* missense variants identified in affected individuals exhibited higher CADD (19) and MPC (https://www.biorxiv.org/content/10.1101/148353v1) scores compared to ultra-rare missense variants in the gnomAD cohort (Figure 2C). All but one missense variant were predicted to be damaging or probably damaging by SIFT (20), PolyPhen-2 (21), and AlphaMissense (22) (Figure 2D). These findings support the pathogenic potential of both LGD and missense variants in *INTS6*.

To further evaluate the potential pathogenic impact of disease-associated missense variants, we analyzed their effects from a structural perspective. The Cryo-EM structure of the Integrator-PP2A complex bound to paused RNAPII revealed that INTS6 directly interacts with INTS8, INTS5, PP2A, and NELFB (Figure 2E). The affected amino acid residues can be categorized into two groups based on their structural locations and roles. Residues T137 and H400 are located at critical interfaces with INTS8 and NELFB, respectively. The side chain of T137 forms hydrogen bonds with Q917, Y940, and Y943 of INTS8, stabilizing the complex, and mutations such as T137I and H400R are likely to disrupt these interactions, impairing the binding of INTS6 to INTS8 and

NELFB (Figure 2E). Several other residues within INTS6 are crucial for maintaining its structural stability (Figure 2E): S91 is located near F55 and forms a hydrogen bond with the side chain of T87; the S91F mutation would eliminate this bond and introduce steric clashes with F55 due to the larger side chain. Similarly, Y111 and R206 form a hydrophilic network with D109, T158, R163, and the backbone of V189, and mutations Y111C and R206C would disrupt these contacts, destabilizing the structural fold. V210 resides within a hydrophobic pocket formed by L171, L173, L175, and L216, and the V210M mutation likely alters this hydrophobic environment. Q228 is positioned in a loop region without substantial residue contacts; however, nearby positively charged residues R39, R167, and R271 could form additional salt bridges with the negatively charged Q228E mutation, potentially altering local electrostatic interactions. Finally, P284 engages in hydrophobic interactions with W283, Y422, Y423, and P426, and replacing P284 with a hydrophilic serine (P284S) would disrupt these hydrophobic contacts, compromising protein folding (Figure 2E). In summary, the NDD-associated missense variants in *INTS6* might impact its function by either disrupting protein-protein interactions or destabilizing the structural integrity required for its activity, likely impairing the role of INTS6 within the Integrator-PP2A complex and contributing to neurodevelopmental pathologies.

***INTS6* monoallelic variants are associated with core features of developmental delay and autism, with a potential male predominance**

To understand *INTS6*-related symptoms, we compiled detailed phenotypic data for 23 affected individuals carrying *INTS6* variants (Table S4). All individuals exhibited neurodevelopmental concerns, with the most common features being language and motor delays, ASD, intellectual disability, and sleep disturbances (Figure 3). Specifically, speech and language problems were reported in 21 out of 23 individuals who underwent language assessments. Among 22 individuals

evaluated for ASD, 17 met the diagnostic criteria for ASD. Motor delays and intellectual disabilities were observed in 14 of 19 individuals. Sleep disturbances were noted in 10 of 16 individuals (Figure 3). Additionally, other neuropsychiatric and neurological issues were identified, including aggressive behavior (7/16), attention-deficit/hyperactivity disorder (ADHD) (6/16), obsessive behavior (5/14), epilepsy (5/14), anxiety (6/17), seizures (6/17), developmental regression (6/22), macrocephaly (4/15), self-injurious behavior (3/12), and depression (2/10) (Figure 3). To investigate whether the phenotypes correlate with the type of variants, we performed unsupervised clustering analysis. The results showed that there was no clear correlation between the clinical features and the type of variants (Figure S3). In summary, these findings highlight a pattern of overlapping neurodevelopmental and neuropsychiatric features in individuals with *INTS6* variants, underscoring the shared phenotypic spectrum among affected individuals.

Interestingly, a notable gender bias was observed in the distribution of *INTS6* variants among affected individuals (Figure 3). Of the 15 individuals with de novo LGD variants or variants of unknown inheritance, 14 were male, with only one female identified. In the single family with inherited *INTS6* variants, the affected male proband inherited the variant from an unaffected mother. Additionally, among the eight probands carrying *de novo* missense variants, six were male. These findings suggest a potential male predominance or female protective effect associated with *INTS6* variants in this disorder. To investigate whether this predominance is linked to differential expression of *INTS6* between males and females, we performed a differential expression analysis using single-cell RNA sequencing data from human brain samples. However, no pronounced sex-related differences in *INTS6* expression were observed (Figure S4A, B).

***Ints6* deficiency interferes neurogenesis and cortical lamination**

To investigate the role of INTS6 in early neurogenesis and cortical development, we generated a

conditional knockout (cKO) model using CRISPR-Cas9 to insert loxP sites flanking exons 5 and 6 of the mouse *Ints6* gene. Mating with Nestin-Cre mice resulted in neural-specific *Ints6* deletion (23) (Figure S5A). Genotypic analysis confirmed the expected Mendelian segregation (Figure S5B), and mRNA analysis at embryonic day 16.5 (E16.5) revealed about a 50% reduction in *Ints6* expression in conditional heterozygous knock out (cHET) mice compared to wild-type (WT) mice, demonstrating efficient gene targeting (Figure S5C). Analysis of offspring genotypes adhered to Mendelian principles. Notably, *Ints6* cKO exhibited postnatal lethality within seven days, whereas cHET grew comparably to WT controls in terms of weight and overall health (Figure S6A).

Given the importance of cortical structure in NDD, we examined the gross morphology of the cerebral cortex. Measurements of the anterior-posterior (A-P) axis and anterior-dorsal (A-D) lengths in cKO mice showed no significant differences compared to WT controls, indicating that *Ints6* deficiency does not alter overall cortical dimensions (Figure S6B-D). In exploring the role of *Ints6* in cortical layer development, we focused on the ventricular zone/subventricular zone (VZ/SVZ), intermediate zone (IZ), and cortical plate (CP) - critical areas for neuronal generation, migration, and organization. DAPI staining and quantification of cell nuclei in E18.5 tissue revealed a thickened VZ/SVZ in the *Ints6* cKO model. Conversely, the CP exhibited significant thinning, indicating impaired neuronal migration or maturation. These changes were not observed in cHET mice (Figure 4A, Figure S7A). These findings underscore the critical role of *Ints6* in proper cortical layer formation.

We further assessed cell identity in the CP using layer-specific neuronal markers. Satb2 predominantly marks upper-layer (L2-L4) neurons, Ctip2 identifies a subset of deep-layer (L5) neurons involved in subcortical projection pathways, and Tbr1 labels early-born, deep-layer (L6) neurons. Although the density of $Tbr1^+$ neurons was comparable, the thickness of L6 was

significantly reduced in cKO mice. In contrast, the thickness and numbers of Satb2^{+} and Ctip2^{+} neurons did not differ significantly between cKO, cHET, and WT mice (Figure 4B-C, Figure S7B). At an earlier developmental stage (E15.5), the region marked by Pax6, indicative of active neural progenitors, was thicker in the *Ints6* cKO mice, whereas the adjacent SVZ marked by Tbr2 region showed no change in thickness (Figure 4D, Figure S7C).

The thickening of SVZ and the thinning of CP L6 suggest a divergence between increased progenitor proliferation and impaired neuron differentiation or survival. To investigate this, we analyzed cortical proliferation in E15.5 mice. While the total number of EdU-positive cells after a 30-minute EdU pulse was unchanged, EdU incorporation in Pax6-positive progenitors was reduced in cKO mice ($p=0.056$), indicating a shortened cell cycle and accelerated proliferation of Pax6-expressing neural stem cells. In contrast, the progenitor of Tbr2-positive intermediate cells was unaffected (Figure 4E, Figure S7D). We performed neurosphere formation assays to further investigate the impact of *Ints6* deficiency on neurogenesis. We recorded and measured the size of neurospheres at 4, 6, and 8 days in vitro, and found that the *Ints6* cKO neurospheres grew more rapidly than those of the WT, which is consistent with our immunofluorescence staining results (Figure 4F, Figure S7E).

Differentiation deficits were evident in E15.5 mice, where 24-hour EdU labeling showed fewer cells exiting the cell cycle, reflecting impaired differentiation of neural stem cells into neurons (Figure 4G). However, cortical neuron migration appeared unaffected, as indicated by the unchanged distribution of EdU^{+} cells across VZ/SVZ, IZ, and CP regions (Figure S7F), as well as between CP layers marked by Satb2, Ctip2, and Tbr1 (Figure S7G). At E18.5, a significant increase in apoptosis was observed in L6 neurons, as indicated by elevated cleaved caspase-3 levels (Figure 4H). These findings suggests that while *Ints6* knockout accelerates neural stem cell proliferation

and thickens the SVZ, it simultaneously hinders differentiation and promotes apoptosis, leading to L6 thinning and disrupted cortical stratification.

Ints6 deficiency disrupts PP2A-RNAPII function

INTS6 is a component of the Integrator complex, a multi-subunit protein complex critical for RNA processing through its interaction with RNAPII (24). To examine the role of INTS6 in RNAPII function and neural development, we performed Cleavage Under Targets and Tagmentation (CUT&Tag) sequencing and RNA immunoprecipitation sequencing (RIP-seq) using RNAPII antibody on E15.5 brain tissues from WT and cKO mice. CUT&Tag analysis revealed a significant enrichment of RNAPII near the transcription start site (TSS) and in distal promoter regions in *Ints6* cKO mice compared to WT (Figure 5A, Table S5). Further examination of the genomic distribution of RNAPII binding peaks showed a notable increase in RNAPII occupancy across the entire gene body in *Ints6* cKO mice (Figure 5B). RIP-seq analysis revealed a shift in RNA-binding distribution between WT and cKO brain tissues. In WT tissues, 35% of reads mapped to untranslated regions (UTRs) (17.6% in 5'UTRs and 17.4% in 3'UTRs) and 37.3% to intronic. In contrast, cKO tissues exhibited 37.8% in UTRs (18.6% in 5'UTRs and 19.2% in 3'UTRs) and 33% in intronic (Figure S8A, Table S6). Genome-wide profiling demonstrated elevated RNAPII accumulation near TSS regions in cKO tissues compared to WT (Figure 5C). Signal density analysis further revealed increased RNAPII occupancy at transcription end sites (TES) and across genomic regions in cKO tissues (Figure 5D). Collectively, these findings suggest that *Ints6* deficiency leads to enhanced RNAPII retention at key gene regulatory regions.

To explore transcriptomic changes, we conducted mRNA sequencing (RNA-seq) on E15.5 mouse brain tissue. Compared to the WT group, the *Ints6* cKO group displayed upregulation of the majority of differentially expressed genes (DEGs) (Table S7). To further refine these findings, we

performed an overlap analysis between DEGs identified by RNA-seq and genes with differential RNAPII binding identified by CUT&Tag. RNA-seq revealed 6,269 DEGs, while CUT&Tag identified 6,779 genes with altered RNAPII binding, with 2,374 genes overlapping between the two datasets (Figure 5E, F). Among the 2,374 differentially expressed genes, 791 were upregulated. Of these, RNAPII occupancy was increased in approximately 661 genes, while the remaining genes showed either decreased occupancy or no substantial change (Figure S8B, C). This finding indicates that RNAPII binding does not always directly correlate with mRNA expression levels, consistent with previous studies (25). Gene Ontology and KEGG pathway enrichment analyses of the overlapping genes revealed significant enrichment in RNA processing-related pathways and cell cycle-related pathways (Figure 5G, H). The binding ability of RNAPII to key regulators of the cell cycle, including Cdk7 (26), Ccnf (27), Mcm5 (28), and Cks2 (29), as well as components of the anaphase-promoting complex/cyclosome (APC/C), such as Cdc16 and Anapc2 (30, 31), were significantly increased in *Ints6* cKO mice (Figure 5I). Consistent with these results, the 3031 overlapping genes between DEGs and RIP-seq data were also significantly enriched in cell cycle-related pathways (Figure S8D-F). We extracted the total mRNA from the cortical tissue and confirmed by qPCR that the expression of cell cycle-related genes in the RIP-seq analysis was downregulated (Figure S8G). These findings are consistent with the disturbed cell cycle observed in neural progenitors of cKO mouse.

To examine the impact of disorder-related *INTS6* variants on PP2A-RNAPII function, we overexpressed plasmids encoding the WT, eight disorder-associated missense and nine disorder-associated LGD variants in HEK293T cells. Our results showed that WT INTS6 significantly suppresses RNAPII Ser2 phosphorylation (Ser2P), consistent with previous findings (32) (Figure 5J, Figure S8H). Overall, all missense and LGD variants exhibited higher Ser2P levels compared

with WT, indicating a failure to suppress Ser2P. However, only two missense variants (V210M, Q228E) and three LGD variants (K326*, R610*, S737*) reached statistical significance with the current number of replicates (Figure 5J, Figure S8H). Since the inhibitor of CDK9 (CDK9i) could lead to a drcease in the phosphorylation of RNAPII, blocking its excessive binding to the target gene (Figure S8I) (32). We then tested whether CDK9i could rescue INTS6-related pathogenesis via neurosphere formation assays. The result showed that CDK9i reversed the over-proliferation of the *Ints6* cKO (Figure 5K, Figure S8J). To further verify the impact of the variants on neural development, we constructed shRNA targeting *Ints6* to knockdown in the brain (Figure S9A). The results of in utero electroporation showed that knockdown of *Ints6* led to a significant increase in Pax6-positive cells, which was consistent with previous results (Figure 4D). By co-expressing WT INTS6 or disorder-related variants plasmid (T137I and H400R), we found that the WT INTS6 could rescue the phenotype of increased Pax6-positive cells, while the two variants located in the key region of the integrator could not rescue (Figure S9B). These findings indicate that disorder-related variants disrupt PP2A-RNAPII function, potentially contributing to neurogenesis defects as observed in the cKO mice.

Ints6 haploinsufficiency lead to social and cognitive impairments in mice

To further explore the role of *Ints6* in disease pathogenesis, we conducted a series of behavioral tests to evaluate common phenotypes associated with *INTS6* variants in humans. Given the lethality of cKO mice, our analyses focused on cHET mice to assess autism-related behaviors and cognition ability. Social behavior, a hallmark of autism, was evaluated using the three-chamber social test. While cHET mice did not show marked social interaction impairment, we observed significantly diminished social novelty preference in cHET mice compared to WT mice (Figure 6A) indicating social novelty impairment. Repetitive and stereotyped behaviors were assessed by

monitoring rearing, grooming, and digging. No significant differences were observed in rearing or digging between *Ints6* cHET and WT mice, and grooming showed only a slight increase, indicating minimal impact on repetitive or stereotyped behaviors (Figure S10A).

Cognitive abilities were assessed using Morris water maze, Y-maze and novel object recognition tests. In the water maze, *Ints6* cHET mice showed reduced learning efficiency and impaired spatial memory retention, as evidenced by less time spent in the target quadrant during the testing phase, while total swimming distance remained unchanged (Figure 6B). In contrast, The Y-maze and novel object recognition tests revealed no significant differences between *Ints6* cHET and WT mice. (Figure S10B, C).

Anxiety-related and hyperactive behaviors were assessed using the elevated plus maze, open field test, and bead-burying test. In the elevated plus maze, *Ints6* cHET mice exhibited significantly increased movement time and distance within the open arms, alongside enhanced movement in the closed arms, suggesting that *Ints6* deficiency may contribute to hyperactivity rather than traditional anxiety-like behavior (Figure 6C). Similarly, in the open field test, the total distance traveled was significantly elevated, although time spent in the central area remained unchanged, further supporting a hyperactive phenotype (Figure 6D). In contrast, the bead-burying test revealed no significant differences in the number of beads buried within 30 minutes (Figure S10D). Taken together, these findings suggest that *Ints6* haploinsufficiency in mice is associated with reduced social novelty preference, impairments in spatial memory and learning, and hyperactivity.

Ints6 deficiency interferes with synapse development

The occurrence of NDD is closely related to changes in the number and morphology of dendritic spines. To investigate the effect of *Ints6* on the development of dendritic spines in neurons, we analyzed dendritic spines in cHET mice crossed with Thy1 EGFP mice with enhanced green

fluorescent protein (EGFP) expression under the control of a modified Thy1 promoter region which contain the sequences required for neuronal expression but lacking the sequences required for expression in non-neural cells expressing (33). At five weeks old, cHET mice displayed a decrease in mushroom and stubby type dendritic spines and an increase in filopodium and thin pseudopodia spines compared to WT mice (Figure 7A). Further analysis using Golgi staining showed a reduction in overall dendritic spines and mature mushroom spines in the cortex layer 2/3 neurons of cHET mice, yet the total dendritic spine count was unaffected (Figure 7B). Considering that the abnormal behaviors observed in *Ints6* cHET mice are associated with hippocampal function, we also examined dendritic spines in the hippocampus and found a similar phenotype to that observed in the cortex (Figure S11A, B).

To further confirm this phenotype, we performed in utero electroporation with GFP and pLKO.1 shRNA (NC) or *Ints6* shRNA plasmids at WT E14.5 mouse embryos. We extracted and cultured the primary neurons from E16.5, and performed fluorescence staining at 18 days *in vitro* (DIV18). Consistent with the above *in vivo* analysis, *Ints6* knockdown substantially reduced the total number of dendritic spines and specifically decreased mushroom-shaped spines compared to the control group (Figure S11C). To validate whether the deficits in spine maturation are related to the PP2A–RNAPII axis, we treated primary neurons from NC and *Ints6* knockdown mice with a CDK9i. The results showed that CDK9i treatment effectively reversed the abnormal spine phenotype induced by *Ints6* knockdown (Figure S11D).

To further investigate the role of *Ints6* in synaptic development, we conducted electron microscopy and immunofluorescence analysis of cortical synapses in WT and cHET mice. Electron microscopy revealed a marked reduction in cortical synapse density in cHET mice. However, synapse contact length did not change compared to WT mice (Figure 7C). Similarly,

immunofluorescence staining for PSD95, a postsynaptic marker, and Synaptophysin, a presynaptic marker, in layer 2/3 of the cortex in 2-month-old mice showed decreased PSD95 and Synaptophysin puncta, along with reduced colocalization of these markers, indicating structural synaptic deficits (Figure 7D). Since synaptic reductions may be attributed to changes in neuronal numbers, we performed NeuN staining on the cortical layer 2/3 of 2-month-old mice. The results revealed no significant difference in neuronal numbers, suggesting that the synaptic deficits are not due to neuronal loss (Figure S12).

To explore the molecular mechanisms underlying *Ints6*'s effect on synaptic development, RNA-seq was performed on cortical tissue from 2-month-old *Ints6* cHET mice. Synaptic Gene Ontology and Annotations (SynGO) analysis of the differentially expressed genes revealed significant enrichment in the synapse, postsynapse, postsynaptic cytoskeleton, and postsynaptic intermediate filament cytoskeleton (Figure 7E, Table S8). Consistent with these findings, KEGG and GO enrichment analyses also highlighted significant involvement of synapse-related pathways (Figure S13A, B). To further strengthen the link between *Ints6* haploinsufficiency and synaptic dysfunction, we isolated synaptic fractions from WT and *Ints6* cHET mice and conducted proteomic analysis. The SynGO analysis of differentially expressed proteins again demonstrated significant enrichment in synapse-related pathways (Figure S13C, Table S9), emphasizing the disruption of key synaptic processes in *Ints6* cHET mice.

The results above indicate that *Inst6* is crucial for dendritic spine maturation. To investigate whether NDD-related missense variants contribute to impaired dendritic spine maturation observed in the *Ints6* cHET mice, we introduced WT and NDD-related variant constructs into embryos *via* electroporation. Overexpression of *INTS6* WT plasmid markedly rescued the reduction of mushroom and stubby. However, none of the disorder-related *de novo* missense

variants were able to restore spine maturation, indicating a loss-of-function effect of these missense variants in synapse development, which is consistent with the *INTS6* LGD variants identified in NDD (Figure 7F).

Discussion

In this study, we combined approches in clinical genetics, structural biology, mouse models, multi-omics, and functional assays to provide compelling evidence linking *INTS6* dysfunction to NDDs. Our findings further establish INTS6 as an essential component of the Integrator complex, mediating neural progenitor proliferation, differentiation, cortical layer formation, and synaptic maturation which contribute to the underlying pathogenesis of INTS-related NDD.

Our analysis of genomic data from large NDD cohorts and followed international multiple center collaborations identified 13 LGD variants from 15 families in *INTS6*, along with eight *de novo* missense variants concentrated in or close to the VWFA domain. The pathogenicity of these missense variants is supported by structural modeling, which suggests that the variants disrupt critical protein-protein interactions or destabilize the structural integrity of INTS6, impairing its function within the Integrator-PP2A complex. However, as these functional predictions have not been directly validated by experimental assays, we cannot conclusively confirm the predicted effects which is a limitation of this study. Nevertheless, the observed inability of the missense variants to reduce RNAPII Ser2 phosphorylation in immunoblotting assays and to rescue dendritic spine maturation in electroporation assays is align with the predicted structural disruptions, further supporting their pathogenicity and loss-of-function effects. Phenotypically, individuals with *INTS6* variants exhibit overlapping features, including language and motor delays, ASD, intellectual disabilities, sleep disturbances and ADHD. These findings underscore the shared phenotypic spectrum of INTS6-associated NDDs and highlight its broad impact on neurodevelopment.

Using a conditional knockout mouse model, we demonstrated that *Ints6* deletion disrupts cortical development, particularly affecting neurogenesis and cortical lamination. Knockout mice showed a thickened VZ/SVZ and thinning of CP, with reduced differentiation and increased apoptosis of CP L6. These defects were associated with impaired RNAPII function and dysregulation of key cell cycle pathways. Furthermore, behavioral assays in cHET mice revealed impairments in social novelty preference, spatial memory, and hyperactivity, alongside structural and functional deficits in dendritic spines and synapses. Molecular studies linked these phenotypes to disruptions in RNAPII activity, PP2A regulation, and altered expression of synaptic genes.

INTS6 was originally identified as a tumor-suppressor protein (34-36), and it is now clear that several additional Integrator subunits are misregulated or mutated in human cancers. The Integrator complex is a multi-subunit protein assembly associated with RNAPII, which plays a crucial role in regulating transcriptional termination, RNA processing, and maintaining genomic stability. It exerts its regulatory function through two main activities: RNA endonuclease activity mediated by INTS11 and protein phosphatase activity facilitated by INTS6 and PP2A. INTS11 cleaves nascent RNA at paused RNAPII sites, preventing nonproductive elongation and ensuring precise transcriptional regulation. Meanwhile, INTS6 recruits PP2A to transcription sites, counteracting the activity of cyclin-dependent kinase CDK9, which controls RNAPII pause-release. This dephosphorylation mechanism ensures that transcription progresses only under appropriate conditions, preserving a balance between gene activation and repression. Disruptions in this balance, such as through mutations in *INTS6* or *INTS11*, lead to aberrant transcriptional elongation, resistance to CDK9 inhibition, and amplified oncogenic transcriptional responses, linking the Integrator complex to both transcriptional regulation and tumor susceptibility (32, 37). In our study, the CDK9 inhibitor effectively reversed the neural development and synaptic

maturation defects caused by Ints6 deficiency. However, this rescue experiment has certain limitations. Notably, we did not perform behavioral assessments in mice to evaluate whether modulation of RNAPII activity translates into functional improvements, which is a critical step in validating the therapeutic potential of this approach. Despite this, our findings suggests that modulating the balance between kinase and phosphatase activities may may represent a promising strategy for treating specific NDDs associated with disrupted Integrator function.

The cryo-EM structures of the Integrator complex have provided substantial insights into its mechanism, revealing three distinct states: pre-termination, post-termination, and inactive (38). In the pre-termination state, the scorpion-like tail module of the Integrator complex positions INTS11 for RNA cleavage while disrupting the DSIF clamp and upstream DNA, triggering the collapse of the transcription bubble and the release of DNA from RNAPII. INTS3 prevents RNAPII from rebinding, ensuring proper termination and preparing the complex for the next cycle. The involvement of INTS6 in regulating the inactive state by occupying the PP2A catalytic site ensures that the complex remains dormant until reactivation is needed. This mechanism of transcription termination is distinct from the torpedo model of 5'-3' exonuclease activity (e.g., XRN2), as it operates independently of XRN2 in many noncoding loci, with INTS11 acting as a dual-function nuclease to degrade RNA and push RNAPII forward (39, 40).

Our RIP-seq and ChIP-seq data revealed increased binding of RNAPII to both RNA and DNA, suggesting altered transcriptional dynamics. RNA-seq further identified upregulated and downregulated genes, indicating a complex transcriptional response associated with INTS6 deficiency. These findings align with previous studies in human cells, where depletion of Integrator subunits led to both up- and down-regulation of protein-coding genes, as observed in HeLa cells depleted of INTS11 (667 upregulated and 616 downregulated genes) (41, 42). This

dual effect suggests that Integrator may play a complex and context-dependent role in transcriptional regulation, which contrasts with simpler models observed in *Drosophila* and *C. elegans* (43). Our data are consistent with the hypothesis that Integrator is crucial for robust transcriptional induction of certain human protein-coding genes, particularly immediate-early genes. Previous studies have shown that INTS1 and INTS11 are recruited to enhancers of these genes, with EGF stimulation enhancing Integrator binding in an ERK1/2-dependent manner (44, 45). When INTS1 or INTS11 is depleted, transcriptional induction of these genes is significantly diminished, which mirrors the transcriptional dysregulation observed in our study. The increased RNAPII binding and altered gene expression in our data suggest that INTS6 may similarly influence transcriptional initiation and elongation at specific loci, potentially through mechanisms involving both RNAPII pausing and enhancer regulation. Our results show that the deletion of INTS6 not only affects the proliferation of neural stem cells but also leads to substantial apoptosis of CP L6 cells in *Inst6* cKO mice. This observation suggests that INTS6 may regulate the expression of different genes at various developmental stages and in different cell types, contributing to distinct cellular outcomes. These results emphasize the need for further investigation into how INTS6 and other Integrator subunits interact with transcriptional machinery to regulate gene expression, especially under stress or developmental conditions.

The Integrator complex plays an indispensable role in early development, tissue morphogenesis, and cell differentiation. In early embryonic stages, it is essential for the regulation of RNAPII pausing and termination. For example, *Ints1* deletion in mouse embryos results in early lethality, likely due to the destabilization of the entire complex (46). Similarly, mutations in *Drosophila* Integrator core components result in mid-to-late larval lethality (47). In zebrafish, mutations in *Ints6* disrupt gastrulation, highlighting the essential role of the Integrator in developmental stages

through the regulation of dorsal organizer genes and the maintenance of proper transcriptional pausing (48). Integrator also plays a role in stem cell maintenance and tissue regeneration, with studies in planarian flatworms demonstrating the importance of Integrator components for stem cell function and tissue renewal. In mice, Integrator is involved in adipocyte differentiation, underscoring its broad biological relevance (49). In neural development, the Integrator complex is particularly crucial in regulating neuronal migration, differentiation, and progenitor cell maintenance. In mouse neuronal progenitor cells, Integrator coordinates cortical neuron migration through interactions with ZFP609 and NIPBL, which regulate transcriptional processes critical for neuron positioning and development (50). In *Drosophila*, Integrator prevents dedifferentiation of intermediate neural progenitors, thereby ensuring proper commitment to terminal cell fates (47).

In humans, mutations in Integrator subunits, including *INTS1* (51, 52), *INTS8* (53), *INTS11* (54) and *INTS13* (55), have been linked to severe NDDs characterized by developmental delays, intellectual disabilities, and structural brain abnormalities. INTS1 and INTS11 are part of the catalytic modules and are essential for RNA cleavage and transcription termination. Mutations in these subunits cause severe cognitive and motor impairments, including cognitive delay, absence of speech, cataracts, glaucoma, and facial dysmorphism (INTS1) or growth restriction, microcephaly, and cerebellar atrophy (INTS11). These defects arise due to improper RNA processing and transcriptional dysregulation. In contrast, INTS8 and INTS6 are involved in the phosphatase module and regulate the recruitment of PP2A to transcription sites, ensuring proper dephosphorylation of RNAPII and transcription factors. Variants in *INTS8* result in severe cognitive delay, speech absence, and motor impairment, while monoallelic variants in *INTS6* lead to milder phenotypes, including speech-language problems, motor delays, and intellectual disability. This suggests that INTS6 may retain partial function despite the monoallelic mutation.

Finally, INTS13, part of the enhancer module, does not affect RNA cleavage or phosphatase activity but regulates enhancer-driven gene expression. Variants in *INTS13* result in oral-facial-digital anomalies and speech abnormalities, highlighting its role in the spatial regulation of transcription. The phenotypes associated with *INTS6* mutations highlight the critical role of the Int–PP2A module and Pol II pausing in human development. Notably, point mutations in PP2A-A have been linked to a broad spectrum of neurodevelopmental disorders (55-57). We hypothesize that transcriptional dysregulation in developing embryos with PP2A-A mutations could be a major pathogenic factor in these disorders. Future studies should focus on understanding the specific contributions of disrupting canonical PP2A ternary complexes versus Integrator-bound PP2A to better elucidate the molecular mechanisms underlying these developmental defects.

Unlike dominant mutations in *INTS6*, biallelic mutations in other *INTS* genes, such as *INTS11*, are associated with neurodevelopmental or neurological disorders. This difference may arise because genes like *INTS11*, which serve as the catalytic core of the Integrator complex, retain sufficient activity at reduced dosage or are buffered by compensatory mechanisms. In contrast, INTS6 likely plays a unique structural or regulatory role, making its function highly dosage-sensitive. Supporting this, neuronal knockdown of *Ints11* produces no apparent phenotype (9), whereas *Ints6* knockdown results in substantial neural abnormalities.

In addition to its well-established role in the phosphatase module of the Integrator complex, INTS6 may also contribute to NDDs through other mechanisms. Recent studies have highlighted direct interactions between INTS6 and INTS3, suggesting that INTS6 may function in ways that are independent of its role in the Integrator complex. Specifically, immunoprecipitation experiments and crystal structure analyses have shown that the C-terminal domain (CTD) of INTS3 mediates interaction with INTS6, possibly facilitating the formation of a heterotrimeric complex composed

of INTS3/INTS6/hSSB1 (58). This interaction may involve multimerization, pointing to a potential alternative function of INTS6 outside the classical transcriptional regulation pathway. This suggests that INTS6 could have roles in cellular processes beyond transcriptional termination, such as genomic stability and DNA repair, through its interactions with hSSB1, a factor involved in DNA damage response (59, 60). Furthermore, INTS6 has been shown to regulate dorsoventral patterning during development by modulating key signaling pathways. For instance, INTS6 disrupts the expression of critical signaling factors, including BMP ligands and mediators of the Wnt signaling pathway, which are essential for proper patterning during embryogenesis (34, 48). These findings underscore the potential role of INTS6 in developmental processes that go beyond its canonical function in transcriptional regulation.

Methods

Sex as a biological variant

Our study exclusively examined male mice because the *INTS6* variants are associated with a potential male predominance.

De novo variants in *INTS1-15* and burden analysis.

De novo likely gene-disruptive and missense variants in the coding regions of INTS1-15 were identified from 32,323 individuals with ASD and 31,085 individuals with ID/DD across five whole-exome and genome sequencing studies. These included a large unpublished ASD cohort, the Simons Foundation Powering Autism Research for Knowledge (SPARK) cohort (12) which comprises 20,646 ASD individuals from 18,405 families with WES/WGS data passing quality control, and four published cohorts: the Simons Simplex Collection (SSC) cohort (13), the Autism Sequencing Consortium (ASC) cohort (14), the MSSNG cohort (15), and the Deciphering

Developmental Disorders (DDD) cohort (2). Potential duplicate samples were excluded if they had the same identifier or carried identical variant(s) originating from related cohorts (e.g., SPAKR, SSC). The variants were re-annotated using ANNOVAR. To evaluate the burden of *de novo* coding variants in INTS1-15, we performed an analysis using *DenovolyzeR* (16), a probabilistic model with default settings. This approach calculates the expected number of *de novo* variants in a given population based on the mutability of a gene and the number of sequenced probands, comparing it to the observed number using a Poisson framework.

Animal

Ints6 $^{flox/flox}$ mice were generated by Cyagen Biotechnology using the CRISPR-Cas9 method, following the strategy outlined in Figure S2A. The strategies for selecting the knockout regions were as follows: 1) Ensure that the sequences of the homology arm and the cKO region were aligned to each other without tandem repeats for PCR screening or sequencing analysis; 2) The homology arm sequence and cKO region have suitable GC content for PCR screening or sequencing analysis; 3) The 3000 bp upstream of the cKO region and the 3000 bp downstream of the cKO region did not show marked similarity to the genome. Considering the above considerations, E5 and E6 are suitable knockout fragments. Nestin-cre mice and Thy1-GFP transgenic mice were provided by Professor Yuan Ling from Central South University, and C57BL/6J mice were obtained from the Medical Genetics Experimental Animal Center of Central South University. Age- and sex-matched littermate pairs were used in the experiments to ensure consistency. Animals were housed in acrylic cages with ad libitum access to water and food and

maintained on a 12-hour light/dark cycle. Environmental conditions were controlled at 22 ± 2°C and 45-55% humidity.

For complete methods, see Supplementary Data Methods.

Statistical analysis

All experiments were performed at least three times. Appropriate statistical tests were applied. Data are presented as mean ± SEM. For two-group comparisons, *P* values were determined from a 2-tailed unpaired (or paired) t-test for normally distributed data, and a Mann-Whitney test for non-normally distributed data. For comparisons among more than two groups, one-way ANOVA with Dunnett's multiple comparisons test was used for normally distributed data, and Kruskal-Wallis test with Dunnett's multiple comparisons test was used for non-normally distributed data. For paired data, the Friedman test with Dunn's multiple comparisons test was applied for non-normally distributed data. Two-way ANOVA with Dunnett's or Bonferroni's multiple comparisons test was used for the analysis of interaction effects between two factors. *P* value < 0.05 was considered statistically significant.

Study approval

Written informed consent was obtained from study participants or their parents or legal guardians, in line with local IRB requirements at the time of collection. The IRB of the Central South University approved this study (IRB#2022-1-3). All animal procedures were approved by the Animal Ethics Committee of Central South University and conducted in accordance with institutional guidelines to minimize animal suffering and adhere to the 3R principle. All animal

experiments were complied with all relevant ethical regulations and were approved by the IRB of Central South University (IRB#2022-2-3).

Data availability

All raw sequencing data generated in this study have been deposited in the NCBI Sequence Read Archive (SRA). The RNA-seq datasets are available under BioProject accession number PRJNA1308459, while the CUT&Tag-seq and RIP-seq datasets are available under BioProject accession number PRJNA1294551. The data values of all graphs and values behind any reports means in the manuscript are provided in the Supporting Data file.

Author contributions

H.G., J.T., K.X., X.P., and X.J. designed and conceived this study. X.P, H.W., X.J., J.C., X.D., C.Q., M.H. and H.H. performed the mouse behavioral and neurogenesis analyses. X.J., X.Z., and S.T. performed genomic analysis and interpreted the genotype and phenotype data. W.Z., Y.Z., Z.M.H., Q.P., F.L., G.C., J.L., and Z.X.H. helped with data interpretation. H.G., J.T., and K.X. supervised the work. X.P., X.J., J.T., H.G., and K.X. wrote and revised the manuscript. The order of the 2 first authors' names was determined by joint decision of these authors. Other authors including I.P., A.K., F.J.K., A.R., R.C., C.S., J.P., B.C., B.I., S.M., G.N., A.M.G., F.F., L.M., L.C., G.B., G.C., B.P., A.S., K.B., J.A.M., C.R., D.B., K.H.K., T.B., Z.S., R.A.J., and E.A.E. contributed and interpreted the genetic and clinical data recruited from an international collaborative network. All authors commented on the manuscript and approved the final manuscript.

Acknowledgments

We are grateful to the families involved in this study. We thank all of the families in SPARK, the SPARK clinical sites, and the SPARK staff. We thank all of the families at the participating SSC

sites, as well as the principal investigators A. Beaudet, R. Bernier, J. Constantino, E. Cook, E. Fombonne, D. Geschwind, R. Goin-Ko- chel, E. Hanson, D. Grice, A. Klin, D. Ledbetter, C. Lord, C. Martin, D. Martin, R. Maxim, J. Miles, O. Ousley, K. Pelphrey, B. Peterson, J. Piggot, C. Saulnier, M. State, W. Stone, J. Sutcliffe, C. Walsh, Z. Warren, and E. Wijsman. We appreciate obtaining access to the phenotypic and genetic data on SFARI Base. Approved researchers can obtain the SSC population dataset described in this study (https://www.sfari.org/resource/simons-simplex- collection/) and the SPARK population dataset described in this study (https:// www.sfari.org/resource/spark/) by applying at https://base.sfari.org. We thank Hartmut Engels for coordinating data collection and assistance. We thank Dr. Isaac Fianu from Max Planck Institute for Multidisciplinary Sciences (Göttingen, Germany) for his critical comments. We thank the Bioinformatics Center of Furong Laboratory, the Bioinformatics Center of Xiangya Hospital, Central South University, and the High-Performance Computing Center of Central South University for their computation support. We also thank Dr. Zhuohua Zhang, Caifang Wang and Dr. Yaohui He from South China University (Hengyang, Hunan, China) for Electron Microscopy and mass spectrometry support, and the Microscopy and Data analysis Platform of the Institude for Advanced Study of Central South Unibersity for assistance. A.K. and F.J.K. from Essen (Germany) are members of the European Reference Network (ERN) ITHACA.

Funding

This study was supported by the STI 2030-Major Project (no. 2021ZD0201704 to H.G.); National Natural Science Foundation of China (nos. 82222025 and 32271141 to H.G.; nos. 82130043, 82330035 and 82361138573 to K.X.; no. 82160219 to W.Z.; no. 82401388 to X.J.); National Key Research and Development Program of China (no. 2021YFA0805200 to Z.H. and J.T.); Hunan Provincial grants (nos. 2023RC1020 and 2023SK2084 to H.G.; nos. 2021SK1010 and

2023SK2114 to K.X.; nos. 2024JJ6545 to X.J.); Jiangxi Province Key Research and Development Project (no. 20232BBG70023 to Y.Z.); Xingdian Project of Yunnan Province (no. XDYC-QNRC-2022-0267 to W.Z.); The REDIA study from the French Ministry of Health (no. PHRC-I 18-38 to G.N.) and Undergraduate Training Programs for Innovation and Entrepreneurship of CSU (X202410533687 to H.H.).

References

1. Thapar A, Cooper M, and Rutter M. Neurodevelopmental disorders. *Lancet Psychiatry.* 2017;4(4):339-46.
2. Kaplanis J, Samocha KE, Wiel L, Zhang Z, Arvai KJ, Eberhardt RY, et al. Evidence for 28 genetic disorders discovered by combining healthcare and research data. *Nature.* 2020;586(7831):757-62.
3. Satterstrom FK, Kosmicki JA, Wang J, Breen MS, De Rubeis S, An JY, et al. Large-Scale Exome Sequencing Study Implicates Both Developmental and Functional Changes in the Neurobiology of Autism. *Cell.* 2020;180(3):568-84 e23.
4. Willsey HR, Willsey AJ, Wang B, and State MW. Genomics, convergent neuroscience and progress in understanding autism spectrum disorder. *Nat Rev Neurosci.* 2022;23(6):323-41.
5. Chen Y, Dawes R, Kim HC, Ljungdahl A, Stenton SL, Walker S, et al. De novo variants in the RNU4-2 snRNA cause a frequent neurodevelopmental syndrome. *Nature.* 2024;632(8026):832-40.
6. Yamamoto J, Hagiwara Y, Chiba K, Isobe T, Narita T, Handa H, et al. DSIF and NELF interact with Integrator to specify the correct post-transcriptional fate of snRNA genes. *Nat Commun.* 2014;5:4263.
7. Greene D, De Wispelaere K, Lees J, Codina-Sola M, Jensson BO, Hales E, et al. Mutations in the small nuclear RNA gene RNU2-2 cause a severe neurodevelopmental disorder with prominent epilepsy. *Nat Genet.* 2025;57(6):1367-73.
8. Nava C, Cogne B, Santini A, Leitao E, Lecoquierre F, Chen Y, et al. Dominant variants in major spliceosome U4 and U5 small nuclear RNA genes cause neurodevelopmental disorders through splicing disruption. *Nat Genet.* 2025;57(6):1374-88.
9. Tepe B, Macke EL, Niceta M, Weisz Hubshman M, Kanca O, Schultz-Rogers L, et al. Bi-allelic variants in INTS11 are associated with a complex neurological disorder. *Am J Hum Genet.* 2023;110(5):774-89.
10. Oegema R, Baillat D, Schot R, van Unen LM, Brooks A, Kia SK, et al. Human mutations in integrator complex subunits link transcriptome integrity to brain development. *PLoS Genet.* 2017;13(5):e1006809.
11. Velmeshev D, Perez Y, Yan Z, Valencia JE, Castaneda-Castellanos DR, Wang L, et al. Single-cell analysis of prenatal and postnatal human cortical development. *Science.* 2023;382(6667):eadf0834.
12. pfeliciano@simonsfoundation.org SCEa, and Consortium S. SPARK: A US Cohort of 50,000 Families to Accelerate Autism Research. *Neuron.* 2018;97(3):488-93.
13. Iossifov I, O'Roak BJ, Sanders SJ, Ronemus M, Krumm N, Levy D, et al. The contribution of de novo coding mutations to autism spectrum disorder. *Nature.* 2014;515(7526):216-21.
14. De Rubeis S, He X, Goldberg AP, Poultney CS, Samocha K, Cicek AE, et al. Synaptic, transcriptional and chromatin genes disrupted in autism. *Nature.* 2014;515(7526):209-15.
15. Trost B, Thiruvahindrapuram B, Chan AJS, Engchuan W, Higginbotham EJ, Howe JL, et

al. Genomic architecture of autism from comprehensive whole-genome sequence annotation. *Cell.* 2022;185(23):4409-27 e18.
16. Ware JS, Samocha KE, Homsy J, and Daly MJ. Interpreting de novo Variation in Human Disease Using denovolyzeR. *Curr Protoc Hum Genet.* 2015;87:7 25 1-7 15.
17. Sobreira N, Schiettecatte F, Valle D, and Hamosh A. GeneMatcher: a matching tool for connecting investigators with an interest in the same gene. *Hum Mutat.* 2015;36(10):928-30.
18. Atkinson EG, Artomov M, Loboda AA, Rehm HL, MacArthur DG, Karczewski KJ, et al. Discordant calls across genotype discovery approaches elucidate variants with systematic errors. *Genome Res.* 2023;33(6):999-1005.
19. Rentzsch P, Witten D, Cooper GM, Shendure J, and Kircher M. CADD: predicting the deleteriousness of variants throughout the human genome. *Nucleic Acids Res.* 2019;47(D1):D886-D94.
20. Vaser R, Adusumalli S, Leng SN, Sikic M, and Ng PC. SIFT missense predictions for genomes. *Nat Protoc.* 2016;11(1):1-9.
21. Adzhubei I, Jordan DM, and Sunyaev SR. Predicting functional effect of human missense mutations using PolyPhen-2. *Curr Protoc Hum Genet.* 2013;Chapter 7:Unit7 20.
22. Cheng J, Novati G, Pan J, Bycroft C, Zemgulyte A, Applebaum T, et al. Accurate proteome-wide missense variant effect prediction with AlphaMissense. *Science.* 2023;381(6664):eadg7492.
23. Betz UA, Vosshenrich CA, Rajewsky K, and Muller W. Bypass of lethality with mosaic mice generated by Cre-loxP-mediated recombination. *Curr Biol.* 1996;6(10):1307-16.
24. Baillat D, Hakimi MA, Naar AM, Shilatifard A, Cooch N, and Shiekhattar R. Integrator, a multiprotein mediator of small nuclear RNA processing, associates with the C-terminal repeat of RNA polymerase II. *Cell.* 2005;123(2):265-76.
25. Henfrey C, Murphy S, and Tellier M. Regulation of mature mRNA levels by RNA processing efficiency. *NAR Genom Bioinform.* 2023;5(2):lqad059.
26. Fisher RP, and Morgan DO. A novel cyclin associates with MO15/CDK7 to form the CDK-activating kinase. *Cell.* 1994;78(4):713-24.
27. Bai C, Richman R, and Elledge SJ. Human cyclin F. *EMBO J.* 1994;13(24):6087-98.
28. Hennessy KM, Lee A, Chen E, and Botstein D. A group of interacting yeast DNA replication genes. *Genes Dev.* 1991;5(6):958-69.
29. Parge HE, Arvai AS, Murtari DJ, Reed SI, and Tainer JA. Human CksHs2 atomic structure: a role for its hexameric assembly in cell cycle control. *Science.* 1993;262(5132):387-95.
30. Townsley FM, and Ruderman JV. Proteolytic ratchets that control progression through mitosis. *Trends Cell Biol.* 1998;8(6):238-44.
31. Jin L, Williamson A, Banerjee S, Philipp I, and Rape M. Mechanism of ubiquitin-chain formation by the human anaphase-promoting complex. *Cell.* 2008;133(4):653-65.
32. Vervoort SJ, Welsh SA, Devlin JR, Barbieri E, Knight DA, Offley S, et al. The PP2A-

Integrator-CDK9 axis fine-tunes transcription and can be targeted therapeutically in cancer. *Cell.* 2021;184(12):3143-62 e32.

33. Feng G, Mellor RH, Bernstein M, Keller-Peck C, Nguyen QT, Wallace M, et al. Imaging neuronal subsets in transgenic mice expressing multiple spectral variants of GFP. *Neuron.* 2000;28(1):41-51.
34. Filleur S, Hirsch J, Wille A, Schon M, Sell C, Shearer MH, et al. INTS6/DICE1 inhibits growth of human androgen-independent prostate cancer cells by altering the cell cycle profile and Wnt signaling. *Cancer Cell Int.* 2009;9:28.
35. Wieland I, Arden KC, Michels D, Klein-Hitpass L, Bohm M, Viars CS, et al. Isolation of DICE1: a gene frequently affected by LOH and downregulated in lung carcinomas. *Oncogene.* 1999;18(32):4530-7.
36. Wieland I, Ropke A, Stumm M, Sell C, Weidle UH, and Wieacker PF. Molecular characterization of the DICE1 (DDX26) tumor suppressor gene in lung carcinoma cells. *Oncol Res.* 2001;12(11-12):491-500.
37. Welsh SA, and Gardini A. Genomic regulation of transcription and RNA processing by the multitasking Integrator complex. *Nat Rev Mol Cell Biol.* 2023;24(3):204-20.
38. Fianu I, Ochmann M, Walshe JL, Dybkov O, Cruz JN, Urlaub H, et al. Structural basis of Integrator-dependent RNA polymerase II termination. *Nature.* 2024;629(8010):219-27.
39. Wagner EJ, Tong L, and Adelman K. Integrator is a global promoter-proximal termination complex. *Mol Cell.* 2023;83(3):416-27.
40. Chen FX, Smith ER, and Shilatifard A. Born to run: control of transcription elongation by RNA polymerase II. *Nat Rev Mol Cell Biol.* 2018;19(7):464-78.
41. Elrod ND, Henriques T, Huang KL, Tatomer DC, Wilusz JE, Wagner EJ, et al. The Integrator Complex Attenuates Promoter-Proximal Transcription at Protein-Coding Genes. *Mol Cell.* 2019;76(5):738-52 e7.
42. Lai F, Gardini A, Zhang A, and Shiekhattar R. Integrator mediates the biogenesis of enhancer RNAs. *Nature.* 2015;525(7569):399-403.
43. Mendoza-Figueroa MS, Tatomer DC, and Wilusz JE. The Integrator Complex in Transcription and Development. *Trends Biochem Sci.* 2020;45(11):923-34.
44. Gardini A, Baillat D, Cesaroni M, Hu D, Marinis JM, Wagner EJ, et al. Integrator regulates transcriptional initiation and pause release following activation. *Mol Cell.* 2014;56(1):128-39.
45. Yue J, Lai F, Beckedorff F, Zhang A, Pastori C, and Shiekhattar R. Integrator orchestrates RAS/ERK1/2 signaling transcriptional programs. *Genes Dev.* 2017;31(17):1809-20.
46. Hata T, and Nakayama M. Targeted disruption of the murine large nuclear KIAA1440/Ints1 protein causes growth arrest in early blastocyst stage embryos and eventual apoptotic cell death. *Biochim Biophys Acta.* 2007;1773(7):1039-51.
47. Zhang Y, Koe CT, Tan YS, Ho J, Tan P, Yu F, et al. The Integrator Complex Prevents Dedifferentiation of Intermediate Neural Progenitors back into Neural Stem Cells. *Cell Rep.*

2019;27(4):987-96 e3.
48. Kapp LD, Abrams EW, Marlow FL, and Mullins MC. The integrator complex subunit 6 (Ints6) confines the dorsal organizer in vertebrate embryogenesis. *PLoS Genet.* 2013;9(10):e1003822.
49. Otani Y, Nakatsu Y, Sakoda H, Fukushima T, Fujishiro M, Kushiyama A, et al. Integrator complex plays an essential role in adipose differentiation. *Biochem Biophys Res Commun.* 2013;434(2):197-202.
50. van den Berg DLC, Azzarelli R, Oishi K, Martynoga B, Urban N, Dekkers DHW, et al. Nipbl Interacts with Zfp609 and the Integrator Complex to Regulate Cortical Neuron Migration. *Neuron.* 2017;93(2):348-61.
51. Krall M, Htun S, Schnur RE, Brooks AS, Baker L, de Alba Campomanes A, et al. Biallelic sequence variants in INTS1 in patients with developmental delays, cataracts, and craniofacial anomalies. *Eur J Hum Genet.* 2019;27(4):582-93.
52. Zhang X, Wang Y, Yang F, Tang J, Xu X, Yang L, et al. Biallelic INTS1 Mutations Cause a Rare Neurodevelopmental Disorder in Two Chinese Siblings. *J Mol Neurosci.* 2020;70(1):1-8.
53. Oegema R, Baillat D, Schot R, van Unen LM, Brooks A, Kia SK, et al. Correction: Human mutations in integrator complex subunits link transcriptome integrity to brain development. *PLoS Genet.* 2017;13(8):e1006923.
54. Kuang H, Li Y, Wang Y, Shi M, Duan R, Xiao Q, et al. A homozygous variant in INTS11 links mitosis and neurogenesis defects to a severe neurodevelopmental disorder. *Cell Rep.* 2023;42(12):113445.
55. Mascibroda LG, Shboul M, Elrod ND, Colleaux L, Hamamy H, Huang KL, et al. INTS13 variants causing a recessive developmental ciliopathy disrupt assembly of the Integrator complex. *Nat Commun.* 2022;13(1):6054.
56. Houge G, Haesen D, Vissers LE, Mehta S, Parker MJ, Wright M, et al. B56delta-related protein phosphatase 2A dysfunction identified in patients with intellectual disability. *J Clin Invest.* 2015;125(8):3051-62.
57. Wallace A, Caruso P, and Karaa A. A Newborn with Severe Ventriculomegaly: Expanding the PPP2R1A Gene Mutation Phenotype. *J Pediatr Genet.* 2019;8(4):240-3.
58. Li J, Ma X, Banerjee S, Baruah S, Schnicker NJ, Roh E, et al. Structural basis for multifunctional roles of human Ints3 C-terminal domain. *J Biol Chem.* 2021;296:100112.
59. Long Q, Ajit K, Sedova K, Haluza V, Stefl R, Dokaneheifard S, et al. Tetrameric INTS6-SOSS1 complex facilitates DNA:RNA hybrid autoregulation at double-strand breaks. *Nucleic Acids Res.* 2024;52(21):13036-56.
60. Jia Y, Cheng Z, Bharath SR, Sun Q, Su N, Huang J, et al. Crystal structure of the INTS3/INTS6 complex reveals the functional importance of INTS3 dimerization in DSB repair. *Cell Discov.* 2021;7(1):66.
61. Offley SR, Pfleiderer MM, Zucco A, Fraudeau A, Welsh SA, Razew M, et al. A

combinatorial approach to uncover an additional Integrator subunit. *Cell Rep.* 2023;42(3):112244.

Figures and Legends

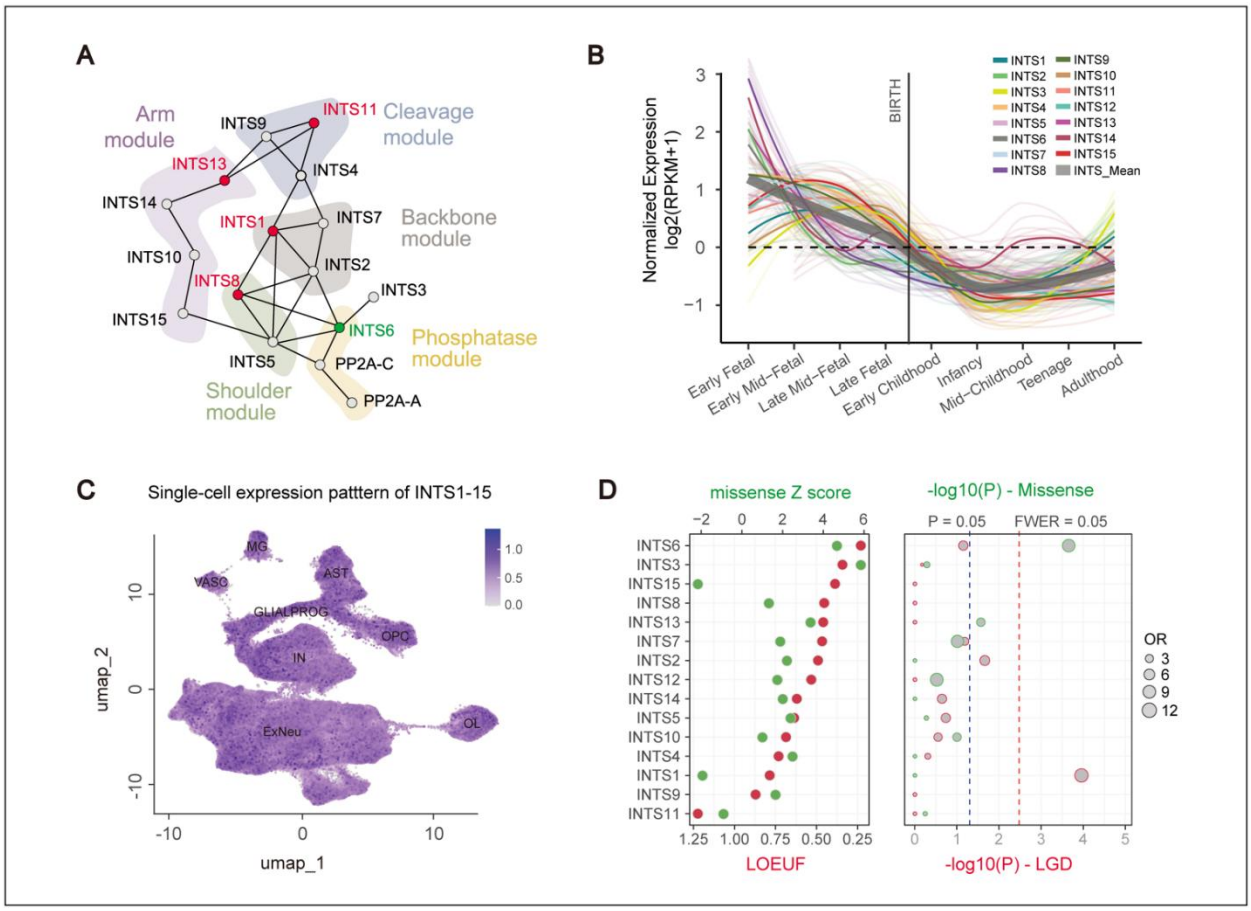

Figure 1. Expression patterns of *INTS1-15* in the human brain and enrichment of *de novo* variants in NDD cohorts. (A) Schematic representation of binary interactions within the Integrator-PP2A complex, adapted from Offley *et al*., Cell Reports (61). Genes highlighted in red represent well-known NDD genes. (B) Normalized expression levels of *INTS1-15* genes across various developmental stages, including fetal stages, birth, infancy, childhood, teenage, and adulthood. Expression data are displayed as $\log_2^{(RPKM+1)}$ values, with color coding highlighting gene-specific trends over time. (C) UMAP plot of single-cell RNA sequencing data showing the average expression patterns of INTS1-15 genes across distinct cell types, including microglia (MG), astrocytes (AST), oligodendrocyte progenitor cells (OPC), excitatory neurons (ExNeu), inhibitory neurons (IN), vascular cells (VASC), and glial progenitors (GLIALPROG). (D) Left: Gene constraint metrics, including LOEUF scores and missense Z scores for loss-of-function (LGD) and missense variants respectively, reflecting the genetic tolerance of INTS genes. Right: Enrichment analysis showing the significance of *de novo* LGD or missense variants in *INTS1-15* among NDD cohorts, compared with expected random occurrences.

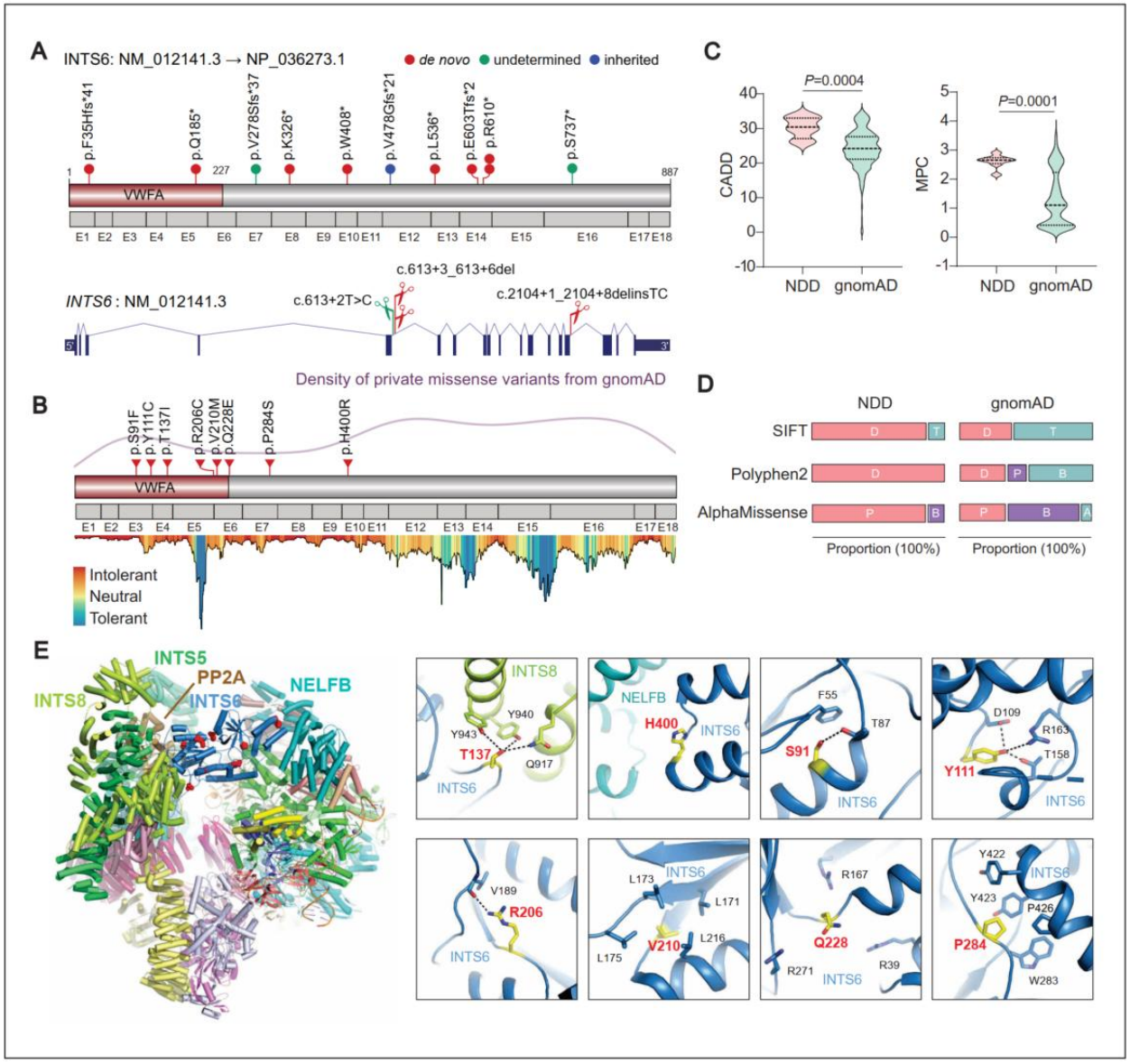

Figure 2. Monoallelic variants in *INTS6* lead to a new NDD syndrome. (A) The distributions of nonsense, frameshift, and splicing variants in *INTS*6 identified in NDDs are shown in a protein model and gene model respectively. (B) The distribution of missense variants in *INTS6* identified in NDDs is shown in a protein model. Protein tolerance landscape for missense variants in *INTS6* was visualized *via* MetaDome20. All variants in INTS6 are predicted to be "intolerant" for aa substitutions. The density plot of ultra-rare missense variants in gnomAD was shown. (C) Comparison of the distribution of CADD and MPC scores between *de novo* missense variants in NDDs and ultra-rare missense variants in gnomAD database. Data are mean ± SEM. *P* values were determined from a 2-tailed unpaired Mann-Whitney test. (D) Comparison of SIFT, Polyphen2 and AlphaMissense prediction between *de novo* missense variants in NDDs and ultra-rare missense variants in gnomAD database. SIFT: D (deleterious), T (tolerated); Polyphen2: D (probably damaging), P (possibly damaging), B (benign); AlphaMissense: P (likely pathogenic), B (likely benign), A (ambiguous). (E) Left: Ribbon diagram of the Integrator-PP2A complex

bound to paused Pol II (PDB:7PKS). The disease-associated protein INTS6 and its interacting proteins are labeled. Right: Close-up view of NDD-related variants on INTS6 (red spheres), highlighting the importance of these residues in mediating protein-protein interactions or maintaining the structural integrity of INTS6.

Phenotype items	Patient index																							Summary	Frequency
	1	2	3	4	5	6	7	8	9	10	11	12	13	14	15	16-1	16-2	17	18	19	21	22	23		
	p.F35Hfs*41	p.Q185*	c.613+2T>C	c.613+3_613+6del	c.613+3_613+6del	p.V278Sfs*37	p.K326*	p.W408*	p.V478Gfs*21	p.L536*	p.E603Tfs*2	p.R610*	p.R610*	c.2104+1_2104+8delinsTC	p.S737*	p.S91F	p.S91F	p.Y111C	p.T137I	p.R206C	p.Q228E	p.P284S	p.H400R		
Gender	M	M	M	M	M	M	M	M	M	M	M	M	M	M	F	M	M	F	M	M	M	M	F	20 M, 3 F	
Inheritance	D	D	U	D	D	U	D	D	I	D	D	D	D	D	U	D	D	D	D	D	D	D	D	19 D, 3 U, 1 I	
Speech-language problems	+	+	+	+	+	+	+	+	+	+	/	+	-	+	+	+	+	+	+	+	+	-	+	20/22	90.9%
Autism spectrum disorder	-	+	+	-	+	+	+	-	+	+	/	-	+	+	+	+	+	+	+	+	-	+	+	17/22	77.3%
Motor delay	+	-	+	+	/	-	-	+	-	-	/	+	+	+	/	+	+	+	/	+	+	/	+	13/18	72.2%
Intellectual disability	+	/	+	/	+	+	-	+	-	-	/	+	+	+	+	/	/	-	+	+	+	-	+	13/18	72.2%
Sleep disturbances	-	-	/	-	/	+	-	+	/	-	/	+	+	/	+	+	+	+	+	+	-	/	/	10/16	62.5%
Aggressive behavior	-	/	-	/	/	+	-	-	/	-	/	+	+	+	+	-	-	+	+	-	-	/	/	7/16	43.8%
ADHD	-	/	-	/	/	+	-	-	/	-	/	+	+	+	-	-	-	+	+	-	-	/	/	6/16	37.5%
Obsessive behavior	-	/	-	/	/	-	-	-	/	-	/	+	/	/	-	+	+	+	/	-	-	/	+	5/14	35.7%
Epilepsy	-	/	/	-	+	-	-	+	/	-	/	+	/	/	+	-	-	/	/	-	-	/	+	5/14	35.7%
Anxiety	-	/	/	+	/	-	-	-	/	-	/	+	-	+	-	-	-	+	-	+	-	/	+	6/17	35.3%
Seizure	-	/	+	-	+	-	-	+	/	-	/	+	-	/	+	-	-	/	-	-	-	/	+	6/17	35.3%
Developmental Regression	-	+	+	-	+	-	-	-	-	-	-	+	-	-	+	-	-	-	+	-	-	/	-	6/22	27.3%
Macrocephaly	+	/	/	-	/	-	+	-	/	-	-	-	/	+	-	-	-	+	/	-	-	/	/	4/15	26.7%
Self-injury behavior	-	/	-	/	/	-	-	-	/	-	/	+	/	/	-	+	+	/	/	-	-	/	/	3/12	25.0%
Depression	-	/	-	-	/	-	-	-	/	/	/	+	/	/	-	/	/	+	/	/	-	/	/	2/10	20.0%

Figure 3. Phenotypic spectrum of individuals carrying *INTS6* variants. ADHD, attention-deficit hyperactivity disorder; M, male; F, female; D, de novo; I, inherited; U, undetermined; +, present; -, absent; /, no data or undetermined.

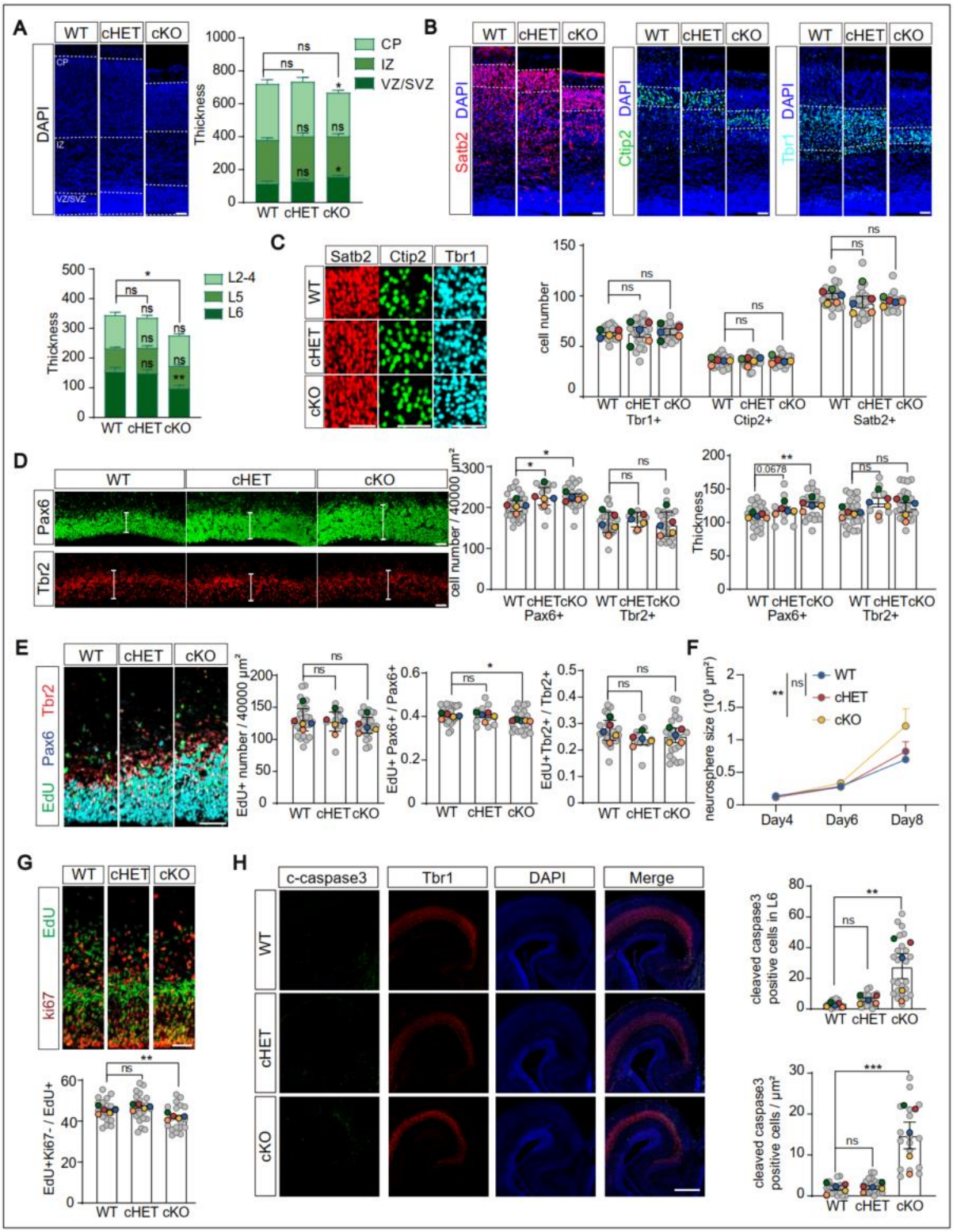

Figure 4. *Ints6* deficiency interferes neurogenesis and cortical lamination. (A) DAPI staining of cortical sections from E18.5 wild-type (WT, n=5), heterozygous (cHET, n=5), and knockout (cKO, n=5) mice, with measurements of cortical thickness. Delineations between the ventricular/subventricular zones (VZ/SVZ),

intermediate zone (IZ), and cortical plate (CP) are indicated by white dashed lines. Scale bar: 50 μm. Data are mean ± SEM. *P* values were determined from one-way ANOVA with Dunnett's multiple comparisons test. (B) Immunofluorescence of E18.5 cortical sections stained for layer-specific markers: Satb2 (red) for layers II-IV, Ctip2 (green) for layer V, and Tbr1 (cyan) for layer VI. Cortical thickness is quantified across genotypes (n=5). Scale bar: 50 μm. Data are mean ± SEM. *P* values were determined from one-way ANOVA with Dunnett's multiple comparisons test. (C) Magnified views of cortical marker staining in B and statistical analysis of cell numbers, n=5, Scale bar: 50 μm. Data are mean ± SEM. *P* values were determined from one-way ANOVA with Dunnett's multiple comparisons test. (D) Immunofluorescence staining for Pax6 (green) and Tbr2 (red) in the SVZ and VZ of E15.5 embryonic brains, comparing WT (n=5), cHET (n=5), and cKO (n=5). Quantitative analysis of cortical thickness and the number of $Pax6^+$ and $Tbr2^+$ cells are presented in adjacent bar charts. Scale bars: 50 μm. Data are mean ± SEM. *P* values were determined from one-way ANOVA with Dunnett's multiple comparisons test. (E) Triple labeling with Pax6 (cyan), Tbr2 (red), and Edu (green) at 0.5 hours post-injection in E15.5 cortices of WT (n=5), cHET (n=5), and cKO mice (n=5), to evaluate proliferative dynamics. Scale bars: 50 μm. Data are mean ± SEM. *P* values were determined from one-way ANOVA with Dunnett's multiple comparisons test. (F) The growth curve of neurosphere cultured in vitro (day4, day6, day8). Data are mean ± SEM. *P* values were determined from two-way ANOVA with Dunnett's multiple comparisons test. (G) Immunofluorescence images of EdU (green) 24h and ki67 (red) staining in WT (n=5), cHET (n=5), and cKO (n=5) cortex at E15.5, showing differentiative capacity. Scale bars: 50 μm. Data are mean ± SEM. *P* values were determined from one-way ANOVA with Dunnett's multiple comparisons test. (H) Representative immunofluorescence images of Tbr1 (red) and cleaved-caspase-3 (green) protein expression in the cerebral cortex tissues from E18.5 embryonic brains (n = 5 per group). DAPI-stained nuclei are shown in blue. Scale bars: 10 μm. Data are mean ± SEM. *P* values were determined from one-way ANOVA with Dunnett's multiple comparisons test. $*P < 0.05$, $**P < 0.01$, $***P < 0.001$, $****P < 0.0001$, ns = no significant. Each biological replicate (mouse) is color-coded; gray dots show individual data point, and colored dots indicate the mean per mouse.

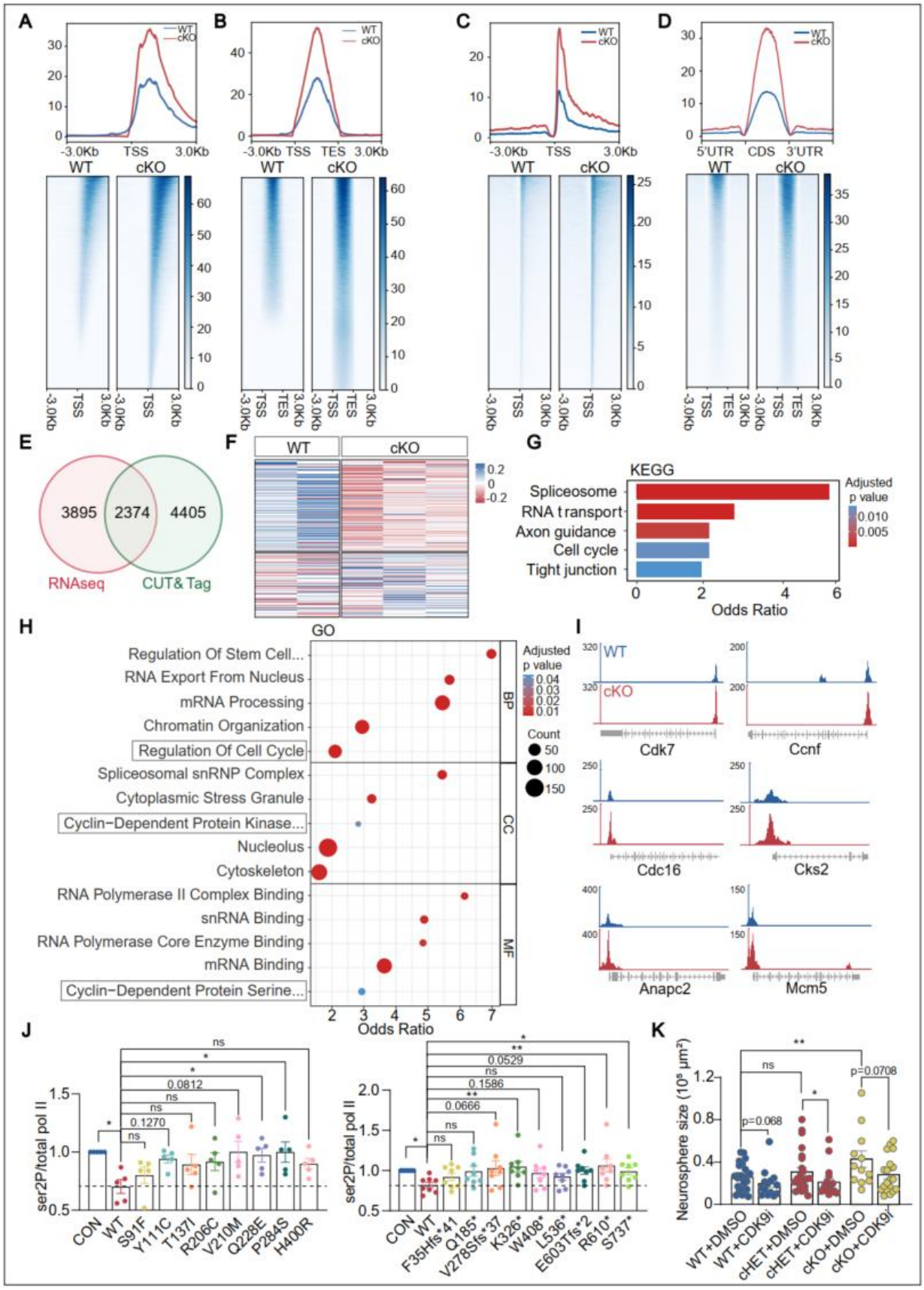
A
B
C
D
WT
cKO
-3.0Kb
TSS
TES
3.0Kb
5'UTR
CDS
3'UTR
E
3895
2374
4405
RNAseq
CUT& Tag
F
G
KEGG
Spliceosome
RNA transport
Axon guidance
Cell cycle
Tight junction
Adjusted p value
Odds Ratio
H
GO
Regulation Of Stem Cell...
RNA Export From Nucleus
mRNA Processing
Chromatin Organization
Regulation Of Cell Cycle
Spliceosomal snRNP Complex
Cytoplasmic Stress Granule
Cyclin−Dependent Protein Kinase...
Nucleolus
Cytoskeleton
RNA Polymerase II Complex Binding
snRNA Binding
RNA Polymerase Core Enzyme Binding
mRNA Binding
Cyclin−Dependent Protein Serine...
BP
CC
MF
Count
I
Cdk7
Ccnf
Cdc16
Cks2
Anapc2
Mcm5
J
ser2P/total pol II
CON
WT
S91F
Y111C
T137I
R206C
V210M
Q228E
P284S
H400R
F35Hfs*41
Q185*
V278Sfs*37
K326*
W408*
L536*
E603Tfs*2
R610*
S737*
K
Neurosphere size (10⁵ μm²)
WT+DMSO
WT+CDK9i
cHET+DMSO
cHET+CDK9i
cKO+DMSO
cKO+CDK9i
p=0.068
p=0.0708

Figure 5. *Ints6* deficiency disrupts PP2A-RNA polymerase II function. (A) Heatmap and spatial distribution of RNA polymerase II binding at transcription start sites (TSS) of genes analyzed by CUT&Tag in WT and cKO E15.5 mice. The color gradient from blue to white indicates decreasing counts in the corresponding areas. (B) Average distribution profile of RNA polymerase II across gene regions, including transcription start and end sites (TSS and TES), in WT and INTS6 cKO mice. (C) Spatial distribution and Heatmap representation of the distance of RNA polymerase II binding around the TSS of RIP-seq genes in WT and cKO mice. The gradient blue-to-white color indicates high-to-low counts in the corresponding region. (D) Average distribution profile of RNA polymerase II across CDS regions of RIP-seq in WT and INTS6 cKO mice. The gradient blue-to-white color indicates high-to-low counts in the corresponding region. (E) Venn diagram illustrating the overlap between DGEs ($p<0.05$) identified in RNAseq and CUT&Tag datasets. (F) Heatmap analysis of the relative expression levels of 2,374 genes in the overlap of RNA-seq and CUT&Tag. Upregulated genes are depicted in blue, while downregulated genes are shown in red. (G) Bar graph depicting enriched KEGG pathways identified from the overlap data. (H) Bubble plot depicting enriched Gene Ontology (GO) terms identified from the overlap data. (I) Browser tracks of CUT&Tag profiles for the genes related to Cell cycle at E15.5 days of embryonic development, comparing expression levels in WT and INTS6 cKO mice. (J) Western blot analysis of total RNA polymerase II and Ser2-phosphorylated forms in HEK293T cells transfected with either wild-type, missense variants INTS6 (n=5) or LGD variants INTS6 (n=8). Data are mean ± SEM. *P* values were determined from Friedman with Dunnett's multiple comparisons test. (K) Statistical analysis of the effects of CDK9i on the growth of WT (n=27, n=14), cHET (n=23, n=18) and cKO (n=12, n=19) neurosphere. Data are mean ± SEM. *P* values were determined from a 2-tailed unpaired *t* test and Mann-Whitney test. $*P < 0.05$, $**P < 0.01$, ns = not significant.

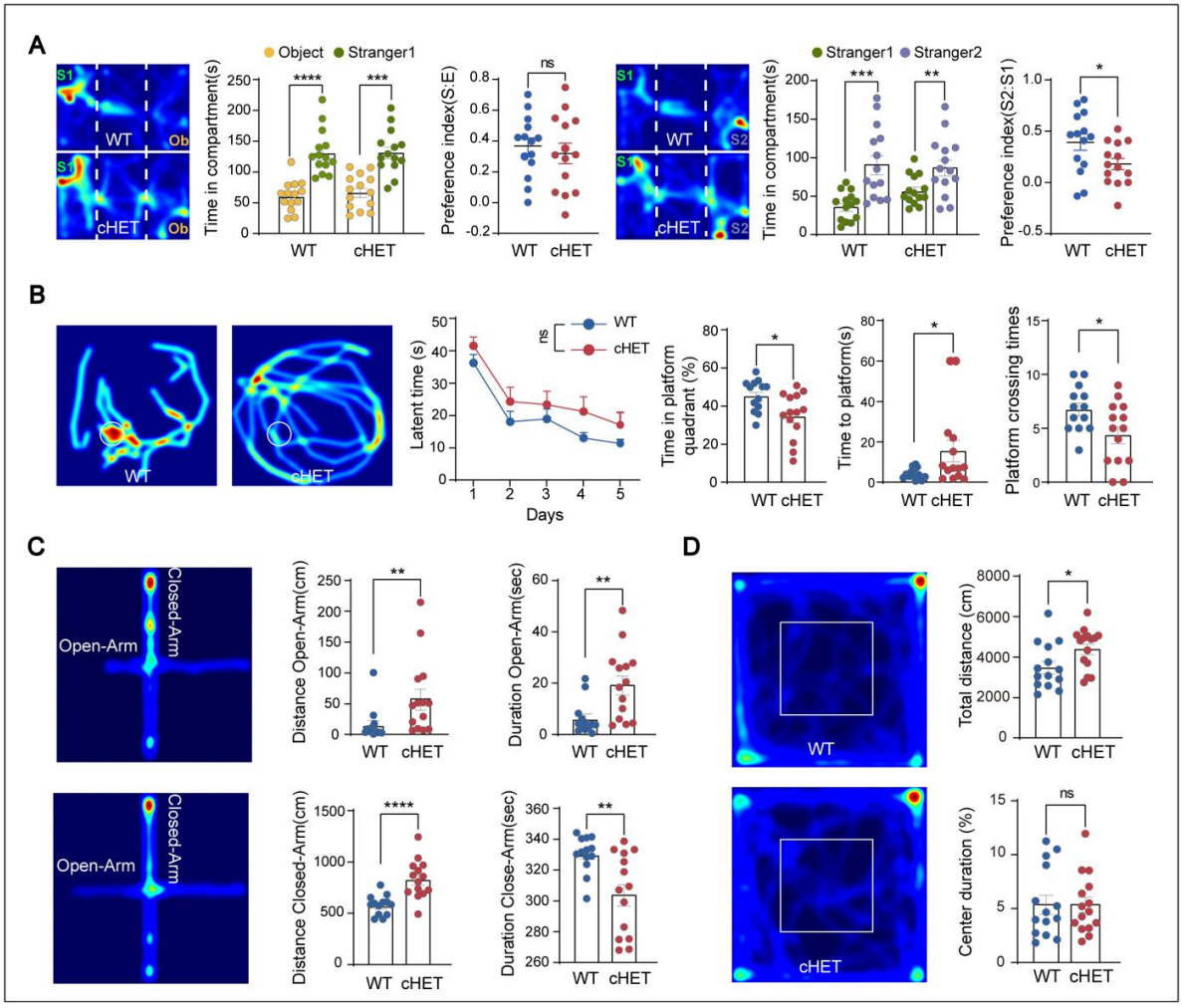

Figure 6. *Ints6* cHET mice lead to social and cognitive impairments. (A) Heatmaps depicting the movement of WT (n=14) or cHET (n=14) mice in a three-chamber social interaction test. Data are mean ± SEM. *P* values were determined from a 2-tailed paired *t* test. Preference scores calculated as (S-E)/(S+E) for social versus empty interactions and (S2-S1)/(S2+S1) for stranger versus original mouse interactions. Data are mean ± SEM. *P* values were determined from a 2-tailed unpaired *t* test. (B) Morris water maze test of spatial learning and memory in *Ints6* cHET mice. Latent time (s) during training trials, time in platform quadrant and distance travelled are measured, n=14. Data are mean ± SEM. *P* values were determined from two-way ANOVA with Bonferroni's multiple comparisons test and a 2-tailed unpaired Mann-Whitney test. (C) Elevated cross maze experiments were performed with wild-type (WT, n=13) and heterozygous (cHET, n=14) mice to evaluate anxiety-related behaviors. The experiments statistically analyzed the movement distance and dwell time in both the open and closed arms of the maze. Data are mean ± SEM. *P* values were determined from a 2-tailed unpaired Mann-Whitney test. (D) Path tracking images from an open field test, showing movement patterns of WT (n=14) and cHET (n=15) mice. Bar graph representing the distance traveled and the time spent in the central area of the open field over 10 minutes. Data are mean ± SEM. *P* values were determined from a 2-tailed unpaired *t* test. **P* < 0.05, ***P* < 0.01, ****P* < 0.001, *****P* < 0.0001, ns = not significant.

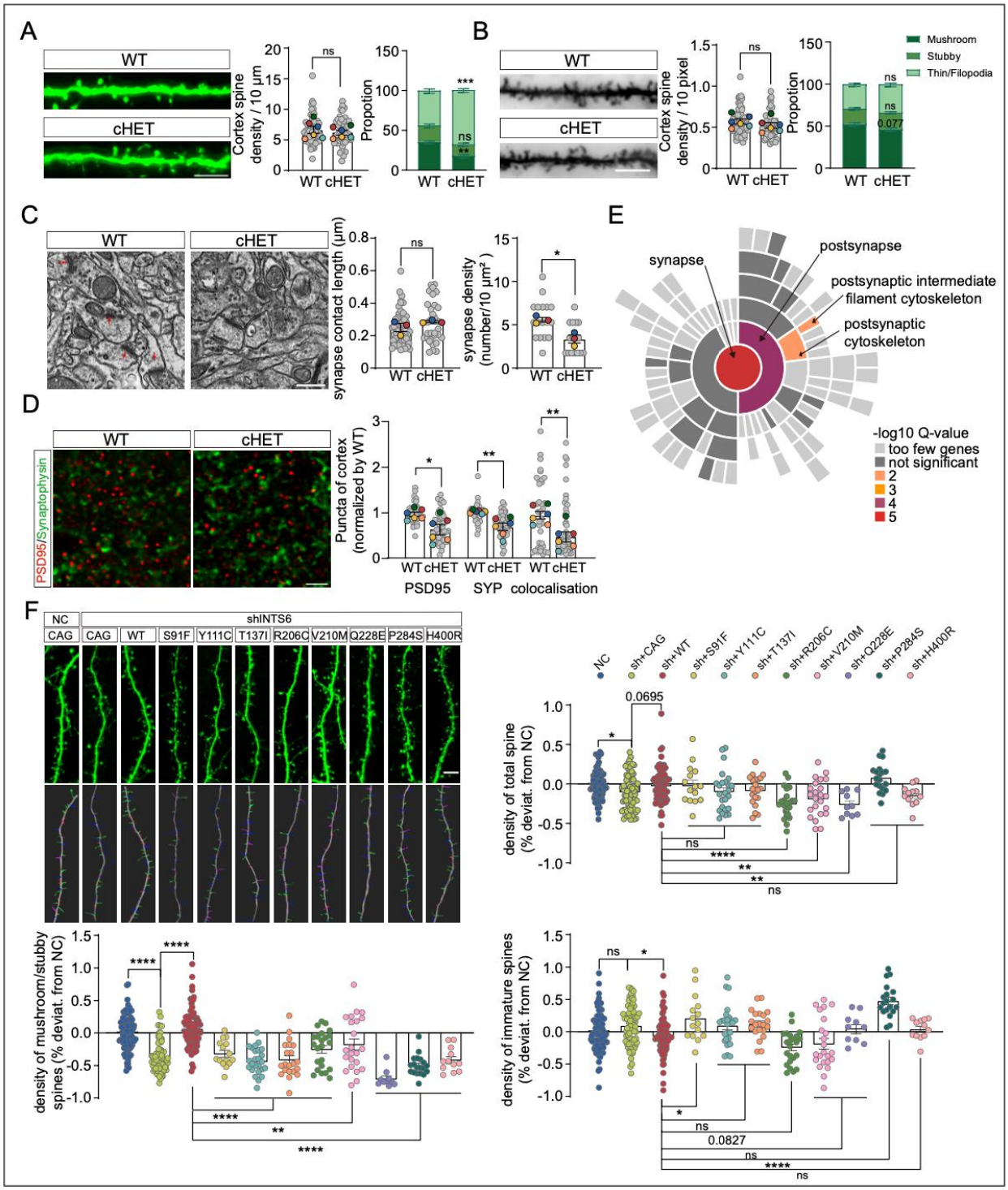

Figure 7. *Ints6* deficiency interferes synapse development. (A) Dendritic spine from 5 weeks mice harboring the Thy1-GFP transgene was stained with an antibody to GFP to enhance the GFP immunolabeling and visualize the morphology and quantified via confocal microscopy, Density of dendritic spine and the three different morphological spine types (stubby, mushroom and thin) expressed as the number of spines normalized to 10 μm of dendritic length, Scale bar: 5 μm. Data are mean ± SEM. *P* values

were determined from a 2-tailed unpaired *t* test. (B) Golgi staining of dendritic spines in the cortex layer 2/3 neurons of WT and cHET mice. Bar graph comparing percentages of spine types (filopodia, stubby, thin, mushroom) between WT and cHET, Scale bar: 100 pixel. Data are mean ± SEM. *P* values were determined from a 2-tailed unpaired Mann-Whitney and *t* test. (C) Brain tissue slices from 7-week-old mice were imaged using electron microscopy to visualize synaptic structures. The red arrow indicates the dense postsynaptic region. ImageJ software was employed to measure the length of the synapse contact and count synapses. Scale bar: 0.5 μm. Data are mean ± SEM. *P* values were determined from a 2-tailed unpaired *t* test. (D) PSD-95 (red) and synaptophysin (green) antibodies were used to stain synapses in the cortical at 2 mouth old mice, graphs depict relative integrated density of PSD-95 and synaptophysin, Scale bar: 2 μm. Data are mean ± SEM. *P* values were determined from a 2-tailed unpaired *t* test. (E) Analysis of SynGO cell components shows overlapping genes represented in a sector diagram. The central sector corresponds to the highest-level term, 'synapse,' with subsequent outward sectors depicting its subclasses. (F) Representative images showing spine density in neurons transfected with wild-type (WT) or variant constructs. The graphs display statistical analyses of total, immature, mushroom, and stubby spine densities, Scale bar: 5 μm. Data are mean ± SEM. *P* values were determined from one-way ANOVA with Dunnett's multiple comparisons test. $*P < 0.05$, $**P < 0.01$, $***P < 0.001$, $****P < 0.0001$, ns = not significant. Each biological replicate (mouse) is color-coded; gray dots show individual data point, and colored dots indicate the mean per mouse.